# Analysis of Fast-Scale Instability in Three-Level T-Type Single-Phase Inverter Feeding Diode-Bridge Rectifier With Inductive Load

Hongbo Cao, *Student Member, IEEE*, Faqiang Wang, *Member, IEEE*, and Jinjun Liu, *Fellow, IEEE*

***Abstract*—In this article, the fast-scale instability in the three-level T-type single-phase inverter feeding diode-bridge rectifier with inductive load (3TSI-DR) is studied. Simulations suggest that such fast-scale instability on switching period scale can increase the harmonic content in the 3TSI-DR, which seriously affects its stable operation. To reveal the mechanism of this fast-scale instability, the state equation of the 3TSI-DR is derived, and state variables are solved based on quasi-static approximation principle. From state equation, the 3TSI-DR is periodic time-varying and piecewise smooth, belonging to Filippov system. Accordingly, the discrete-time mapping model of the 3TSI-DR is established, Filippov method is used for obtaining monodromy matrix, and Floquet theory is applied to explore instability mechanism. Theoretical results indicate that the fast-scale instability of the 3TSI-DR is caused by period-doubling bifurcation. Moreover, the Floquet multiplier sensitivities of different circuit parameters are calculated to identify key parameters; via comparing theoretical analyses with simulations, the unstable angle ranges of the fast-scale instability are given, and the stability boundaries in various parameter spaces are discussed. All these can provide design-oriented information for optimizing the 3TSI-DR to avoid instability due to period-doubling bifurcation. Finally, experimental results agreeing with simulations are presented to verify the correctness of theoretical analyses.**

***Index Terms*—Diode-bridge rectifier with inductive load, fast-scale instability, Floquet multiplier sensitivities, period-doubling bifurcation, stability boundaries, three-level T-type single-phase inverter.**

## NOMENCLATURE

| | |
|---|---|
| $E$ | DC input voltage. |
| $C_{\rm dc}$ | DC supporting capacitor. |
| $C_0$ | Inverter-side filter capacitor. |
| $L_1$ | Inverter-side filter inductor. |
| $L_2$ | Rectifier-side inductor. |
| $R$ | Rectifier-side resistor. |
| $R_{pi}$ | Control loop resistor. |
| $V_{\rm ref}$ | Amplitude of the reference voltage. |
| $V_{\rm tri}$ | Amplitude of the carrier voltage. |
| $\omega$ | Angular frequency of the reference voltage. |
| $f$ | Frequency of the reference voltage. |
| $f_s$ | Switching frequency. |
| $T_s$ | Switching period. |
| $I_s$ | Reverse saturation current of the diode. |
| $V_T$ | Thermal voltage of the diode. |
| $N_e$ | Emission coefficient of the diode. |
| $k_{\rm dc}$, $k_0$ | DC sampling factor and ac sampling factor. |
| $k_p$, $k_i$ | Proportional and integral parameters. |
| $i_{\rm dc}$ | DC input current. |
| $i_{L1}$ | Inverter-side filter inductor current. |
| $i_{\rm M}$ | Inverter-side ac output current. |
| $i_{L2}$ | Rectifier-side inductor current. |
| $i_1$, $i_2$, $i_3$, $i_4$ | Currents through the diodes $\rm D_1$, $\rm D_2$, $\rm D_3$, $\rm D_4$. |
| $v_0$ | Inverter-side ac output voltage. |
| $v_{\rm dc}$, $v_{\rm dc1}$ | Terminal voltages of the supporting capacitors. |
| $v_{\rm diff}$ | Deviation voltage. |
| $v_{\rm ref}$ | Reference voltage. |
| $v_{\rm con}$, $v_{\rm con1}$ | Modulation voltages. |
| $v_{\rm tri}$ | Carrier voltage. |
| $v_{ge1}$, $v_{ge2}$ | Gate signals of the switches $\rm S_1$ and $\rm S_2$. |
| $v_{ge3}$, $v_{ge4}$ | Gate signals of the switches $\rm S_3$ and $\rm S_4$. |
| $\mathbf{x}(t)$ | State variables. |
| $\Delta\mathbf{x}(t)$ | Disturbance quantity at any time $t$. |
| $\mathbf{A}_n$ | Coefficient matrix. |
| $\mathbf{B}_1$, $\mathbf{B}_2$, $\mathbf{B}_3$ | Input vectors. |
| $\mathbf{\Phi}_i$ | State transition matrix. |
| $\mathbf{\Phi}_{n1}$, $\mathbf{\Phi}_{n2}$, $\mathbf{\Phi}_{n3}$ | Substate transition matrixes. |
| $\mathbf{\Phi}_{\rm cycle}$ | Monodromy matrix. |
| $\mathbf{G}_i$ | Saltation matrix. |
| $\mathbf{I}$ | Identity matrix. |
| $h_i(\mathbf{x}(t),t)$ | Transition condition. |
| $\mathbf{p}_i$ | Normal vector of the transition condition. |
| $\mathbf{f}_{i-}$ | Value of the state equation before the time $t_i$. |
| $\mathbf{f}_{i+}$ | Value of the state equation after the time $t_i$. |
| $d_{n1}$, $d_{n2}$ | Duty cycles. |
| $\lambda_i$ | Floquet multiplier. |
| ${H_i}^{\rm T}$ | Left eigenvector of the Floquet multiplier $\lambda_i$. |
| $Q_i$ | Right eigenvector of the Floquet multiplier $\lambda_i$. |

Manuscript received 30 January 2022; revised 21 April 2022 and 10 June 2022; accepted 19 July 2022. Date of publication 28 July 2022; date of current version 6 September 2022. Recommended for publication by Associate Editor E. Babaei. *(Corresponding author: Faqiang Wang.)*

The authors are with the State Key Laboratory of Electrical Insulation and Power Equipment, School of Electrical Engineering, Xi'an Jiaotong University, Xi'an 710049, China (e-mail: caohongbo@stu.xjtu.edu.cn; faqwang@mail.xjtu.edu.cn; jjliu@mail.xjtu.edu.cn).

Color versions of one or more figures in this article are available at https://doi.org/10.1109/TPEL.2022.3194697.

Digital Object Identifier 10.1109/TPEL.2022.3194697

## I. Introduction

POWER electronic circuits play an increasingly important role in renewable energy resources and energy storage technologies because of the power conversion capabilities [1]. However, power electronic circuits belong to nonlinear circuits and are prone to generate a variety of instability behaviors under certain parameter conditions [2]–[7]. So far, research on the instability behaviors of power electronic circuits has developed from dc–dc converters [6]–[10] as well as power factor correction converters [11]–[13] to dc–ac converters [14]–[16]. Existing research results have declared that various instability behaviors are likely to break out in inverter circuits. From their manifestations, these complex instability behaviors in inverter circuits can be classified as bifurcation and chaos, among which the bifurcation is the way to chaos [17]. According to the time scale, the bifurcation instabilities are categorized into slow-scale instability and fast-scale instability [18], [19]. The slow-scale instability takes place on the line period scale, whereas the fast-scale instability occurs on the switching period scale [18]–[20]. For another, based on the dynamical mechanism, these various bifurcation instabilities can be divided into Hopf bifurcation, period-doubling bifurcation, and saddle bifurcation [20]. Besides, other interesting bifurcation phenomena have also been reported in inverter circuits, such as Neimark–Sacker bifurcation [21], boundary collision bifurcation [22], synchronous bifurcation [23], etc. Note that, as stated in [17]–[23], these complex instability behaviors will deteriorate the work environment of the loads and pollute the power supplies so as to seriously affect the stable operation of the inverter circuits. Hence, these instability behaviors should be avoided in actual applications. To be sure, aforementioned abundant and excellent research results can help engineers to understand these various instability behaviors in depth, and are valuable to provide some significant references for the stable operation of the traditional two-level inverters in practical engineering.

As aforesaid, the previous research works about the instability behaviors in the field of the inverter circuits are only focus on the traditional two-level inverters with resistive loads [14]–[23], which are all linear loads. However, as stated in [20], industrial loads are usually a combination of complex nonlinear loads in actual situations. In addition, the three-level T-type inverter can change the dc input voltage from the solar panel, battery or fuel cell panel into an alternating current (ac) output voltage [24], [25]. Compared with the traditional two-level inverters, the three-level T-type inverters have the merits of less distortion and higher efficiency [26], [27]. Hence, the three-level T-type inverter has been commonly employed as ac power supply in actual engineering, especially being used to power nonlinear loads [28], [29]. Nevertheless, it is inevitable that the three-level T-type inverters with nonlinear loads are strongly nonlinear systems and are more likely to exhibit instability phenomena [30], [31]. But few studies have been done on instability behaviors of the three-level T-type inverters with nonlinear loads.

In practical applications, power electronic appliances have become common nonlinear loads in inverter circuits [32]. Most of the power electronic appliances are electrical devices, which are manufactured based on the single-phase diode-bridge rectifiers [33], such as notebook computers, televisions, compact fluorescent lamps, etc. Also, they are generally small rated, and installed throughout the low-voltage distribution network [32], [33]. So, stably supplying power for these diode-bridge rectifier-based power electronic appliances is a significant work worth researching. As described in [34]–[36], the diode-bridge rectifier with inductive load often is used to represent a class of nonlinear loads in power electronic systems. Factually, it is a typical power electronic system when the diode-bridge rectifier with inductive load is adopted as the nonlinear load for the three-level T-type single-phase inverter. Specially, the following two points need to be paid attention to. First, when is powered by a periodic ac voltage source, the diode-bridge rectifier with inductive load can display a pinched hysteresis loop passing through the origin in the voltage versus current plane [37], [38]. That is, the diode-bridge rectifier with inductive load not only can represent a class of power electronic nonlinear loads, but also can stand for a class of memristive nonlinear loads [38]. Second, the three-level T-type single-phase inverter feeding diode-bridge rectifier with inductive load (3TSI-DR) is a strongly nonlinear system owing to the combined action of the switching elements and the diode-bridge rectifier-based load. That is, the 3TSI-DR probably gives rise to a variety of instability behaviors, which seriously affect its stable operation in practice. Therefore, studying instability behaviors in the 3TSI-DR and revealing the instability mechanism are significant for the stability enhancement of the 3TSI-DR.

At present, time-domain simulations and dynamic theories are two vital pathways to research the instability behaviors of inverter circuits. Among them, the time-domain simulation is an effective approach to display the characteristic curves of power electronic systems and to verify the correctness of theoretical results, but it is incompetent to explain dynamical mechanism of various instability behaviors in depth and unable to provide comprehensive design-oriented information for optimizing the systems. In terms of theoretical techniques, both the modeling of the switches and the processing of the discrete-characteristic are primary issues to be solved for investigating the instability behaviors appearing in power electronic systems. Up to now, some modeling methods have been applied to describe the dynamics of power electronic systems, such as the harmonic state-space (HSS) modeling [39]–[42] and the discrete-time mapping modeling [17], [20]. As stated in [40]–[42], the HSS model is mainly applied to analyze the harmonic dynamics in the power electronic systems with consideration of harmonic coupling, and its precision depends on the harmonic orders considered, where the higher the harmonic orders, the more accurate the model. However, the calculation process will become cumbersome as the model size is expanded [40]. Besides, the calculation process of the HSS modeling is completed via convolution calculation in the frequency-domain and two different frequency components will generate new coupling component, so that the HSS model obviously carries more redundant information if it is used to explore the dynamical mechanism of the instability in the 3TSI-DR on the switching period scale [41], [42]. Indeed, the discrete-time mapping model is suitable for detailed analysis on the complex

dynamics of power electronic systems, especially can accurately describe the high-frequency dynamical information of power electronic systems and intuitively predict the oscillations of power electronic systems occurring on switching period scale [18], accordingly, it has become an important method to model the inverter circuits [20]. Currently, the unified discrete-time mapping modeling method [2], [17] and the improved discrete-time mapping modeling method [18], [20] have been widely used to analyze the instability behaviors on switching period scale in inverter circuits. Nevertheless, the modeling and analytic methodology in [2] and [17], exploring the mechanism of instability phenomena with the aid of the unified discrete-time mapping model and Jacobian matrix, are only applicable for the systems whose coefficient matrix in the state equation is reversible. The approach, via using an improved discrete-time mapping model and Jacobian matrix in [18] and [20], is only suitable for the systems whose coefficient matrix in the state equation is time-invariant. Unfortunately, the coefficient matrix in the state equation of the 3TSI-DR is nonreversible due to the PI regulation, and is periodic time-varying owing to the diode-bridge rectifier-based load. Hence, the aforementioned theoretical methodologies fail to explore the mechanism of the instability behaviors in the 3TSI-DR. Attentively, if there are several discontinuities in the state equation of a piecewise smooth system, it can be considered as the Filippov system [43], [44]. By means of introducing the saltation matrix, the Filippov system can be approximately transformed into a continuous smooth system, which makes the modeling and analyzing of the Filippov system simplified. Indeed, the 3TSI-DR is a piecewise nonlinear smooth periodic time-varying system and belongs to Filippov system.

This article aims to reveal the dynamical mechanism of the instability behaviors in the 3TSI-DR, to present design-oriented information for optimizing the 3TSI-DR, and to promote the study on the instability behaviors in the multilevel inverter circuits. Contributions can be summarized as follows. The fast-scale instability on switching period scale in the 3TSI-DR is recognized, and the mechanism of the fast-scale instability in the 3TSI-DR is revealed. The Floquet multiplier sensitivities of the different circuit parameters are calculated to identify the key parameters affecting the stability of the 3TSI-DR; the unstable angle ranges of the fast-scale instability with circuit parameters changing are given; the stability boundaries in various parameter spaces are discussed; so as to provide design-oriented information to ensure stable operation of the 3TSI-DR in an adequately wide parameter range. Also, analysis methodology via combining Filippov method and Floquet theory to explore the fast-scale instability in the 3TSI-DR can provide theoretical guidance for the study on the instability behaviors in the multilevel inverters with nonlinear loads.

The rest of this article is as follows. In Section II, operation principle of the 3TSI-DR is introduced and its simulation results are shown. In Section III, the state equation of the 3TSI-DR is derived, the discrete-time mapping model of the 3TSI-DR is established, the mechanism of the fast-scale instability is revealed, and the normalized Floquet multiplier sensitivities of different circuit parameters are calculated. In Section IV, the unstable angle ranges of the fast-scale instability as circuit parameters change are given and the stability boundaries in various parameter spaces are discussed. In Section V, experimental verifications are provided. Finally, Section VI concludes this article.

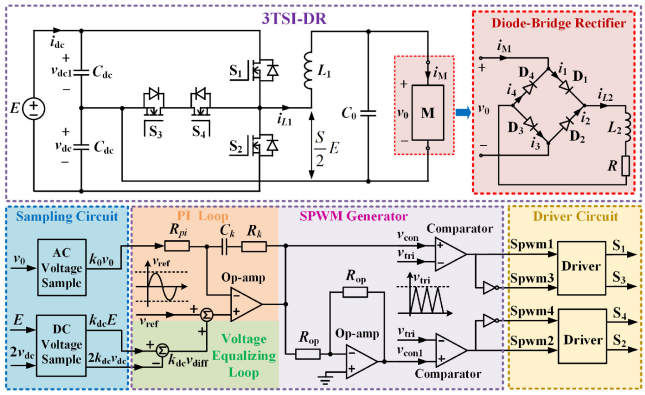


Fig. 1. Circuit schematic of the 3TSI-DR.

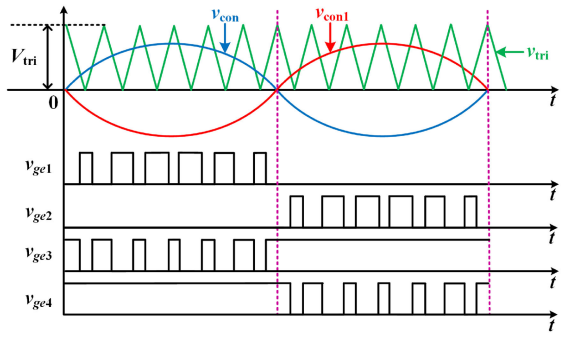


Fig. 2. Unipolar SPWM of the 3TSI-DR.

## II. Circuit Topology and Simulations

### A. Topology and Operation Principle

The circuit schematic of the 3TSI-DR is shown in Fig. 1, where T-type bridge is constituted of four switches ($S_1$, $S_2$, $S_3$, and $S_4$). The inverter-side filter is formed by inductor $L_1$ and capacitor $C_0$; the diode-bridge rectifier, consisting of a diode bridge ($D_1$, $D_2$, $D_3$, and $D_4$) as well as a series inductor $L_2$ and resistor $R$, is selected as the nonlinear load and is marked with "M." Also, sampling circuit, control circuit, and driver circuit are shown in Fig. 1, respectively. The PI regulation is used in controller, and the voltage equalizing loop is added onto PI loop to adjust and balance the dc input voltage of the 3TSI-DR.

The unipolar sinusoidal pulsewidth modulation (SPWM) strategy of the 3TSI-DR is shown in Fig. 2. The modulation voltage $v_{\rm con}$ is outputted through PI regulator, and $v_{\rm con1} = -v_{\rm con}$. The carrier voltage $v_{\rm tri}$ in one switching period can be given as

$$v_{\rm tri} = \begin{cases} 2V_{\rm tri}\frac{t}{T_s}, 0 < t < \frac{T_s}{2} \\ 2V_{\rm tri}\frac{(T_s - t)}{T_s}, \frac{T_s}{2} < t < T_s \end{cases} \quad (1)$$

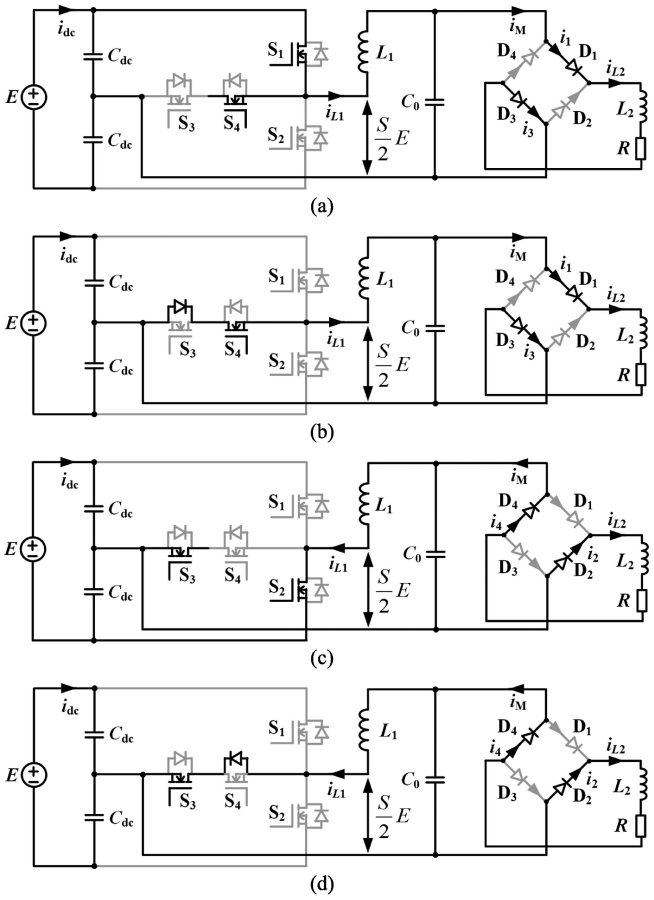


Fig. 3. Equivalent circuits of the 3TSI-DR in possible operation modes. (a) Forward active mode ($i_{L1}>0$). (b) Forward freewheeling mode ($i_{L1}>0$). (c) Reverse active mode ($i_{L1}<0$). (d) Reverse freewheeling mode ($i_{L1}<0$).

where $T_s$ and $V_{\rm tri}$ stand for the switching period and the amplitude of the carrier voltage, respectively. The reference voltage is $v_{\rm ref} = V_{\rm ref}\sin(\omega t)$, where $\omega$ is the angular frequency of the reference voltage and $V_{\rm ref}$ is its amplitude.

As shown in Fig. 2, the gate signal $v_{ge1}$ of switch $S_1$ is complementary to the gate signal $v_{ge3}$ of switch $S_3$. While the gate signal $v_{ge2}$ of switch $S_2$ lags the gate signal $v_{ge1}$ of switch $S_1$ by 180°, and is complementary to the gate signal $v_{ge4}$ of switch $S_4$. Hence, the equivalent circuits of the 3TSI-DR in possible operation modes are displayed in Fig. 3. The followings are the operation modes of the 3TSI-DR.

1) *Forward active mode ($i_{L1}>0$):* As shown in Fig. 3(a), switch $S_1$ is turned ON; switches $S_2$ and $S_3$ are turned OFF; although switch $S_4$ is driven, it does not form a circuit loop. The T-type bridge-arm voltage is $+0.5E$, i.e., $S = 1$. At this time, the inverter-side ac output voltage $v_0$ is in the positive half cycle, so diodes $D_1$ and $D_3$ conduct through the forward voltage while diodes $D_2$ and $D_4$ are blocked through the reversal voltage.
2) *Forward freewheeling mode ($i_{L1}>0$):* As shown in Fig. 3(b), switches $S_1$ and $S_2$ are turned OFF; switch $S_3$ acts as the freewheeling diode; switch $S_4$ is turned ON. The T-type bridge-arm voltage is 0, i.e., $S = 0$. At this time, the inverter-side ac output voltage $v_0$ is in the positive half cycle, thereby diodes $D_1$ and $D_3$ conduct through the forward voltage while diodes $D_2$ and $D_4$ are blocked through the reversal voltage.
3) *Reverse active mode ($i_{L1}<0$):* As shown in Fig. 3(c), switches $S_1$ and $S_4$ are turned OFF; switch $S_2$ is turned ON; although switch $S_3$ is driven, it does not form a circuit loop. The T-type bridge-arm voltage is $-0.5E$, i.e., $S = -1$. At this time, the inverter-side ac output voltage $v_0$ is in the negative half cycle, so diodes $D_2$ and $D_4$ conduct through the forward voltage, while diodes $D_1$ and $D_3$ are blocked through the reversal voltage.
4) *Reverse freewheeling mode ($i_{L1}<0$):* As shown in Fig. 3(d), switches $S_1$ and $S_2$ are turned OFF; switch $S_3$ is turned ON; switch $S_4$ acts as the freewheeling diode. The T-type bridge-arm voltage is 0, i.e., $S = 0$. At this time, the inverter-side ac output voltage $v_0$ is in the negative half cycle, thereby diodes $D_2$ and $D_4$ conduct through the forward voltage, while diodes $D_1$ and $D_3$ are blocked through the reversal voltage.

Hence, the T-type bridge-arm voltage changes among three levels, that is, $+0.5E$, 0, and $-0.5E$. There is

$$S = \begin{cases} 1, \text{S}_1 \text{ and S}_4 \text{ are turned on, S}_2 \text{ and S}_3 \text{ are turned off} \\ 0, \text{S}_3 \text{ and S}_4 \text{ are turned on, S}_1 \text{ and S}_2 \text{ are turned off} \\ -1, \text{S}_2 \text{ and S}_3 \text{ are turned on, S}_1 \text{ and S}_4 \text{ are turned off} \end{cases}. \tag{2}$$

TABLE I
CIRCUIT PARAMETERS OF THE 3TSI-DR

| Circuit Parameters | Values |
|---|---|
| DC input voltage and DC supporting capacitor ($E$, $C_{\rm dc}$) | 24V, 4.7mF |
| Amplitude and frequency of the reference voltage ($V_{\rm ref}$, $f$) | 1V, 50Hz |
| Amplitude and frequency of the carrier voltage ($V_{\rm tri}$, $f_s$) | 1.2V, 8kHz |
| Inverter-side filter inductor and capacitor ($L_1$, $C_0$) | 1mH, 68μF |
| Rectifier-side inductor and resistor ($L_2$, $R$) | 2mH, 4.5Ω |
| Reverse saturation current of the diode ($I_s$) | 2.1μA |
| Thermal voltage of the diode ($V_T$) | 25.27mV |
| Emission coefficient of the diode ($N_e$) | 2.34 |
| DC and AC sampling factors ($k_{\rm dc}$, $k_0$) | 0.1, 0.1 |
| Control loop parameters ($R_{pi}$, $k_i$) | 5kΩ, 200 |

### B. Circuit Simulations

For the purpose of stable supply power for the diode-bridge rectifier-based nonlinear load, the 3TSI-DR is designed to transform the 24-V dc input voltage into an ac output voltage with 10-V amplitude and 50-Hz line frequency. Here, as the proportion parameter $k_p$ changes, some PSpice simulations are executed to explore the possible instability behaviors occurring in the 3TSI-DR. The PSpice simulation data are imported into MATLAB software in order to facilitate image editing. The values of circuit parameters in PSpice simulation are listed in Table I.

Fig. 4 shows that when the proportion parameter is chosen as $k_p = 4.4$ (i.e., $R_k = 22\ \text{k}\Omega$), the 3TSI-DR can work in the stable state. From Fig. 4(b), the curve in the inverter-side ac output voltage $v_0$ versus the inverter-side ac output current $i_{\rm M}$ plane displays a typical pinched hysteresis loop. Then, via employing fast Fourier transform (FFT) tool in PSpice software, the total

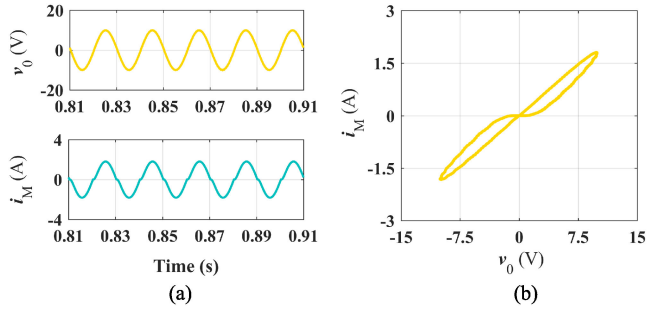


Fig. 4. PSpice simulations of the 3TSI-DR under $k_p = 4.4$ (i.e., $R_k = 22$ kΩ). (a) Time-domain waveforms of the inverter-side ac output voltage $v_0$ and ac output current $i_M$. (b) $v_0$-$i_M$ curve.

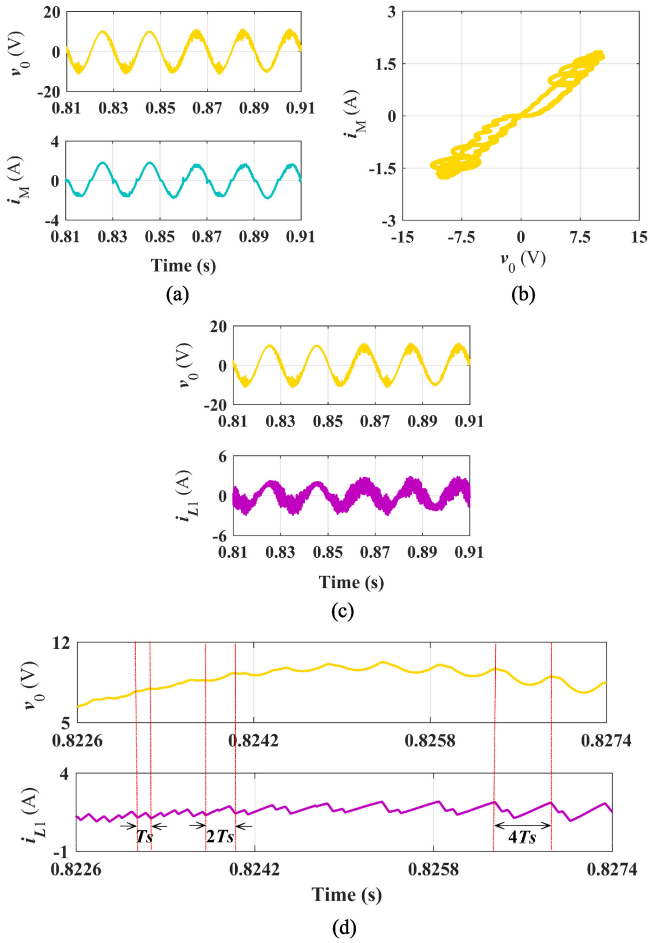


Fig. 5. PSpice simulations of the 3TSI-DR under $k_p = 14.8$ (i.e., $R_k = 74$ kΩ). (a) Time-domain waveforms of the inverter-side ac output voltage $v_0$ and ac output current $i_M$. (b) $v_0$-$i_M$ curve. (c) Time-domain waveforms of $v_0$ and the inverter-side filter inductor current $i_{L1}$. (d) Close-up view of $v_0$ and $i_{L1}$.

harmonic distortion (THD) of the inverter-side ac output voltage $v_0$ can be got as 0.54%, and the THD of the inverter-side ac output current $i_M$ can be got as 6.71%.

Fig. 5 indicates that when the proportion parameter is increased to $k_p = 14.8$ (i.e., $R_k = 74$ kΩ), the 3TSI-DR will lose stability. Fig. 5(a) displays that there are obvious oscillations at the peaks and troughs of the simulation curves $v_0$ and $i_M$. By using FFT tool, the THD of $v_0$ and $i_M$ can be obtained as 8.06% and 7.40%, respectively. Fig. 5(b) shows that the curve $v_0$-$i_M$ is located at the first and third quadrants as well as passing through the origin. That is, the diode-bridge rectifier-based load still maintains the essential pinched hysteresis characteristic but with undesired distortion. In order to obtain the periods of the oscillations occurring in the 3TSI-DR, the portraits of the inverter-side ac output voltage $v_0$ and the inverter-side filter inductor current $i_{L1}$ are displayed in Fig. 5(c). Also, a partial enlarged view of Fig. 5(c) is given in Fig. 5(d), where the obvious oscillations can be observed. In particular, from Fig. 5(d), the observed oscillation in the 3TSI-DR is an instability behavior on the switching period scale, whose oscillation period is always an integer multiple of the switching period. This instability on switching period scale is termed fast-scale instability. Clearly, when the fast-scale instability occurs, the operation period of the 3TSI-DR changes from period-1 (equal to the switching period) to period-2 (equal to twice the switching period), and then evolving into period-4 (equal to four times the switching period).

With the proportion parameter $k_p$ continuing to increase, the fast-scale instability occurring in the 3TSI-DR becomes more serious. Fig. 6 shows the simulation results of the 3TSI-DR under $k_p = 16$ (i.e., $R_k = 80$ kΩ). From Fig. 6(a) and (b), the work environment of the diode-bridge rectifier-based load becomes worse. By employing FFT tool, the THDs of $v_0$ and $i_M$ are got as 10.74% and 9.24%, respectively. Notably, from Fig. 6(c) and (d), the developed fast-scale instability is discovered in the 3TSI-DR with respect to $k_p = 16$. At this moment, the operation period of the 3TSI-DR changes from period-2 (equal to twice the switching period) to period-4 (equal to four times the switching period), i.e., the 3TSI-DR loses the period-1 mode in the whole line period. As indicated in [18], such fast-scale instability that occurs during the whole line period is named the full-bifurcation instability.

Obviously, as the proportion parameter $k_p$ increase, the 3TSI-DR is going to experience the fast-scale instability, which will increase the harmonic content of the 3TSI-DR so as to deteriorate the work environment of the diode-bridge rectifier-based nonlinear load; hence, this fast-scale instability seriously affects the stable operation of the 3TSI-DR.

## III. Theoretical Analyses

The simulation results in Section II-B have suggested that the fast-scale instability on switching period scale will break out in the 3TSI-DR depending upon the changing proportion parameters. In this section, the mechanism of the fast-scale instability in the 3TSI-DR will be revealed theoretically.

At first, the state equation of the 3TSI-DR will be derived, and state variables will be solved. From the state equation, the 3TSI-DR is a piecewise smooth periodic time-varying system and belongs to Filippov system, thus its discrete-time mapping model of the 3TSI-DR will be established. Then, via combining Filippov method and Floquet theory, the mechanism of the fast-scale instability in the 3TSI-DR will be revealed according to the trajectories of the Floquet multipliers in the complex plane.

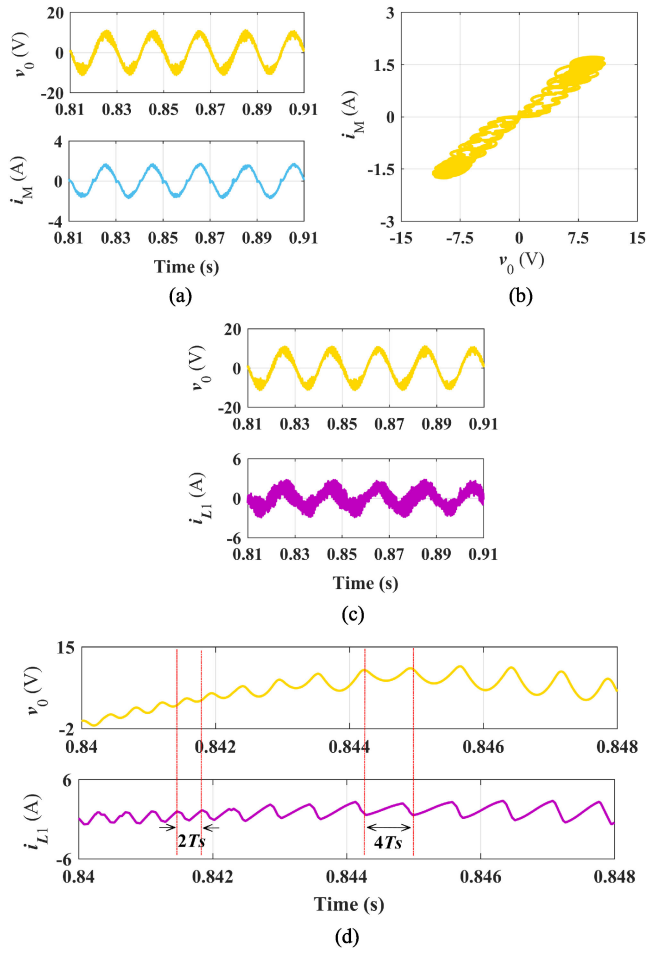


Fig. 6. PSpice simulations of the 3TSI-DR under $k_p = 16$ (i.e., $R_k = 80$ kΩ). (a) Time-domain waveforms of the inverter-side ac output voltage $v_0$ and ac output current $i_M$. (b) $v_0$-$i_M$ curve. (c) Time-domain waveforms of $v_0$ and the inverter-side filter inductor current $i_{L1}$. (d) Close-up view of $v_0$ and $i_{L1}$.

At last, the key parameters affecting the stability of the 3TSI-DR will also be identified.

### A. State Equation

As shown in Fig. 1, via applying Kirchhoff's voltage law (KVL) and Kirchhoff's current law (KCL), respectively, the circuit equations of the T-type bridge can be derived as

$$\frac{di_{L1}}{dt} = -\frac{v_0}{L_1} + \frac{S}{2L_1}E \tag{3}$$

$$\frac{dv_0}{dt} = \frac{i_{L1}}{C_0} - \frac{i_M}{C_0}. \tag{4}$$

According to the work in [45], the reverse saturation current $I_s$, the emission coefficient $N_e$, and the thermal voltage $V_T$ can be used to describe the constitutive relation of four diodes ($D_1$, $D_2$, $D_3$, and $D_4$) in diode-bridge rectifier, and there is

$$i_k = I_s(e^{2\rho v_k} - 1) \tag{5}$$

where $\rho = 1/(2N_eV_T)$, $k = 1, 2, 3, 4$. $v_k$ and $i_k$ represent the voltage across the diode $D_k$ and the current flowing through it, respectively. In the diode-bridge rectifier, the voltages across

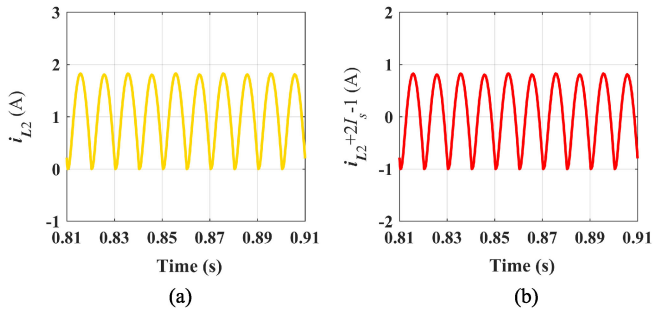


Fig. 7. For the 3TSI-DR under $k_p = 4.4$ (i.e., $R_k = 22$ kΩ), simulation results of (a) the rectifier-side inductor current $i_{L2}$ and (b) $i_{L2}+2I_s-1$.

each pair of parallel diodes are equal (i.e., $v_1 = v_3$ and $v_2 = v_4$). By applying KCL at the two nodes connected to the diode $D_1$, the following equations can be given:

$$i_M = i_1 - i_2 \tag{6}$$

$$i_{L2} = i_1 + i_2. \tag{7}$$

Also, applying KVL to the loop formed by the voltage $v_0$, diodes $D_1$ and $D_2$, and to the loop formed by the voltage $v_0$, diode $D_1$, inductor $L_2$, resistor $R$, and diode $D_3$, then one can get

$$v_2 = v_1 - v_0 \tag{8}$$

$$2v_1 = v_0 - v_{L2} - v_R. \tag{9}$$

By combining (5), (6), and (8), we can derive as follow:

$$v_1 = \frac{1}{2\rho}\ln\frac{i_{L2} + 2I_s}{2I_s e^{-\rho v_0}\cosh(\rho v_0)}. \tag{10}$$

From (5), (7), (8), and (10), the constitutive relationship between the current flowing through the diode-bridge rectifier (i.e., the inverter-side ac output current $i_M$) and its terminal voltage (i.e., the inverter-side ac output voltage $v_0$) can be got as

$$i_M = (i_{L2} + 2I_s)\tanh(\rho v_0). \tag{11}$$

Since the rectifier-side inductor current $i_{L2}$ is related to the inverter-side ac output voltage $v_0$. By substituting (10) into (9) and according to $v_{L2} = L_2(di_{L2}/dt)$, we can obtain

$$\frac{di_{L2}}{dt} = -\frac{Ri_{L2}}{L_2} + \frac{1}{\rho L_2}\ln(2I_s\cosh(\rho v_0)) - \frac{1}{\rho L_2}\ln(i_{L2}+2I_s). \tag{12}$$

The third term in the right-hand side of (12) can be depicted as

$$-\frac{1}{\rho L_2}\ln(i_{L2} + 2I_s) = -\frac{1}{\rho L_2}\ln(i_{L2} + 2I_s - 1 + 1). \tag{13}$$

The simulation waves of the rectifier-side inductor current $i_{L2}$ and $i_{L2}+2I_s-1$ are displayed in Fig. 7(a) and (b) by using PSpice software. From Fig. 7, one can yield the following condition:

$$-1 < i_{L2} + 2I_s - 1 \le 1. \tag{14}$$

Then, on account of (14), via performing Taylor expansion for the right-hand side of (13) and taking the first term,

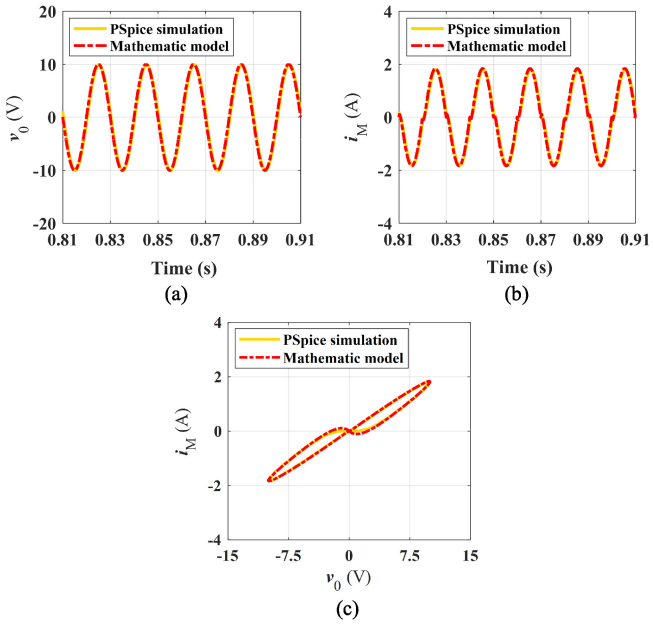


Fig. 8. Comparisons between PSpice simulation and mathematical model. (a) Input voltage $v_0$ of the diode-bridge rectifier. (b) Input current $i_{\rm M}$ of the diode-bridge rectifier. (c) $v_0$-$i_{\rm M}$ curve.

we can get

$$-\frac{1}{\rho L_2}\ln(i_{L2}+2I_s)\approx-\frac{1}{\rho L_2}(i_{L2}+2I_s-1). \tag{15}$$

From (11), (12), and (15), a simplified mathematical model (16), which can be used to describe the diode-bridge rectifier with inductive load exactly, is proposed as follows:

$$\begin{cases} i_{\rm M}=(i_{L2}+2I_s)\tanh(\rho v_0) \\ \frac{di_{L2}}{dt}=-\frac{1}{\rho L_2}((\rho R+1)i_{L2}-\ln(2I_s\cosh(\rho v_0))+2I_s-1) \end{cases}. \tag{16}$$

The comparisons between mathematical model and simulation result of the diode-bridge rectifier with inductive load are displayed in Fig. 8, which suggests that the mathematical model (16) is almost consistent with the simulation results. Hence, the mathematical model (16) can be used to describe the dynamical characteristics of the diode-bridge rectifier-based load shown in Fig. 1, effectively.

Notably, the diode-bridge rectifier with inductive load can exhibit a typical pinched hysteresis loop passing through the origin in its input voltage $v_0$ versus its input current $i_{\rm M}$ plane. As proven in [46], any two-terminal circuit can be regarded as a memristor emulator, if it can display a pinched hysteresis loop passing through the origin in the voltage versus current plane when is powered by a periodic ac voltage source or ac current source. Besides, the mathematical model (16) conforms to the definition about a class of the generalized memristors, as indicated in [46] and [47]. Hence, on basis of a certain mathematical sense, the diode-bridge rectifier with inductive load can be considered as the first-order generalized memristor emulator [37], [38]. That is to say, the diode-bridge rectifier-based load shown in Fig. 1 can represent both a power electronic nonlinear load and a memristive nonlinear load.

By applying KVL for the voltage equalizing loop, we can get

$$v_{\rm dc1}+v_{\rm dc}=E. \tag{17}$$

For the forward active mode of the 3TSI-DR, as shown in Fig. 3(a), that is, $i_{L1}>0$, by applying KCL one can obtain

$$C_{\rm dc}\frac{dv_{\rm dc1}}{dt}=i_{\rm dc}-i_{L1}. \tag{18}$$

Also, for the reverse active mode of the 3TSI-DR, as shown in Fig. 3(c), that is, $i_{L1}<0$, by applying KCL one can get

$$C_{\rm dc}\frac{dv_{\rm dc}}{dt}=i_{\rm dc}+i_{L1}. \tag{19}$$

Then, defining that the deviation voltage is $v_{\rm diff}=E-2v_{\rm dc}$, and according to (17)–(19), we can calculate as follows:

$$\frac{dv_{\rm diff}}{dt}=-\frac{2}{C_{\rm dc}}i_{L1}. \tag{20}$$

For PI control loop, $k_p=R_k/R_{pi}$ is the proportional parameter and $k_i=1/(C_kR_{pi})$ is the integral parameter, thus we can get

$$\begin{aligned}\frac{dv_{\rm con}}{dt}=&k_p\left(k_{\rm dc}\frac{dv_{\rm diff}}{dt}+\frac{dv_{\rm ref}}{dt}-k_0\frac{dv_0}{dt}\right)\\&+k_i(k_{\rm dc}v_{\rm diff}+v_{\rm ref}-k_0v_0).\end{aligned} \tag{21}$$

From (21), the following equation can be obtained:

$$\begin{aligned}\frac{dv_{\rm con}}{dt}=&k_pk_{\rm dc}\frac{dv_{\rm diff}}{dt}-k_pk_0\frac{dv_0}{dt}+k_ik_{\rm dc}v_{\rm diff}-k_ik_0v_0\\&+k_p\omega V_{\rm ref}\cos(\omega t)+k_iV_{\rm ref}\sin(\omega t).\end{aligned} \tag{22}$$

Therefore, by combining (3), (4), (16), (20), and (22), the state equation of the 3TSI-DR, described by state variables ($i_{L1}$, $i_{L2}$, $v_0$, $v_{\rm diff}$, $v_{\rm con}$), can be derived as

$$\begin{cases} \frac{di_{L1}}{dt} = -\frac{v_0}{L_1}+\frac{S}{2L_1}E \\ \frac{di_{L2}}{dt} = -\frac{1}{\rho L_2}((\rho R+1)i_{L2}-\ln(2I_s\cosh(\rho v_0))+2I_s-1) \\ \frac{dv_0}{dt} = \frac{i_{L1}}{C_0}-\frac{(i_{L2}+2I_s)\tanh(\rho v_0)}{C_0} \\ \frac{dv_{\rm diff}}{dt} = -\frac{2i_{L1}}{C_{\rm dc}} \\ \frac{dv_{\rm con}}{dt} = -\frac{2k_pk_{\rm dc}}{C_{\rm dc}}i_{L1}-\frac{k_pk_0}{C_0}(i_{L1}-(i_{L2}+2I_s)\tanh(\rho v_0)) \\ \qquad +k_ik_{\rm dc}v_{\rm diff}-k_ik_0v_0+k_p\omega V_{\rm ref}\cos(\omega t) \\ \qquad +k_iV_{\rm ref}\sin(\omega t) \end{cases}. \tag{23}$$

### B. Discrete-Time Mapping Model

For the 3TSI-DR, the topology sequence of the stable period-1 is displayed in Fig. 9(a), where $v_{\rm con1}=-v_{\rm con}$. Clearly, during a switching period, when $v_{\rm con}>v_{\rm con1}$, the 3TSI-DR will operate in the topology sequence-1 of the stable period-1, as displayed in Fig. 9(b), where $d_{n1}$ and $d_{n2}$ are the duty cycles of the 3TSI-DR; when $v_{\rm con}<v_{\rm con1}$, the 3TSI-DR will operate in the topology sequence-2 of the stable period-1, as shown in Fig. 9(c). Attentively, for the 3TSI-DR during a line period, the topology sequence-1 in the first half-line period and the topology sequence-2 in the second half-line period are symmetric. Beside, as indicated in [18] and [20], the fast-scale instability of the inverter system on the switching period scale always occurs

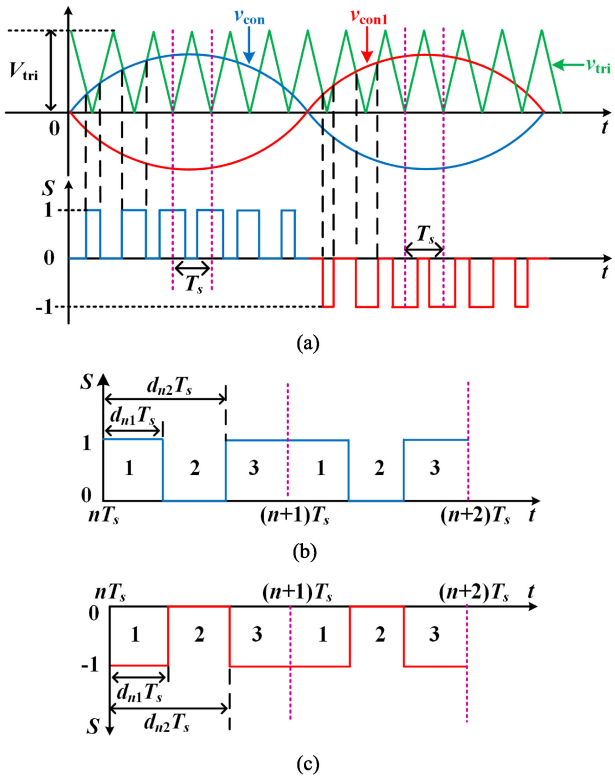


Fig. 9. (a) Topology sequence of the stable period-1, $v_{con1} = -v_{con}$. (b) When $v_{con} > v_{con1}$, the 3TSI-DR works in the topology sequence-1. (c) When $v_{con} < v_{con1}$, the 3TSI-DR works in the topology sequence-2.

first near the middle time of each half-line period, then it is going to be distributed around the peaks and troughs of the ac output voltage. As expected, one can observe from Figs. 5(a) and 6(a) that the fast-scale instability of the 3TSI-DR occurs around the peaks and troughs of the inverter-side ac output voltage $v_0$ and ac output current $i_M$. Therefore, the mechanism of the fast-scale instability in the 3TSI-DR can be investigated within the half-line period [18], so that the case when the 3TSI-DR operates in the topology sequence-1 from $nT_s$ to $(n+1)T_s$, as drawn in Fig. 9(b), is analyzed in the following.

Owing to the inverter-side ac output voltage $v_0$ is periodic time-varying and the switching frequency (8 kHz) is much larger than the line frequency (50 Hz), one can estimate that the inverter-side ac output voltage is constant during each switching period. Thereby, in the switching period $[nT_s, (n+1)T_s]$ $(n>0)$, the instantaneous value of the inverter-side ac output voltage $v_0$ can be replaced by its average value. From Fig. 9(b), when the 3TSI-DR operates in the topology sequence-1, the average value of $v_0$ can be obtained as

$$v_0 = (d_{n1} + (1 - d_{n2}))\frac{E}{2}. \tag{24}$$

Assume that the integration constant corresponding to the initial value of the rectifier-side inductor current $i_{L2}$ is equal to 1. From (23), the instantaneous value of $i_{L2}$ can be calculated as

$$i_{L2} = e^{-\frac{\rho R+1}{\rho L_2}t} + \frac{1}{\rho R+1}(\ln(2I_s\cosh(\rho v_0)) - 2I_s + 1). \tag{25}$$

Since the switching period is small, based on the quasi-static approximate principle, the instantaneous value of $i_{L2}$ in the switching period $[nT_s, (n+1)T_s]$ can be substituted by its value at the moment $nT_s$, and there is

$$i_{L2} = e^{-\frac{\rho R+1}{\rho L_2}nT_s} + \frac{1}{\rho R+1}(\ln(2I_s\cosh(\rho v_0)) - 2I_s + 1). \tag{26}$$

In addition, according to Fig. 9(b), when the 3TSI-DR operates in the topology sequence-1, the 3TSI-DR has two transition moments during each switching period, i.e., the 3TSI-DR actually has three subcircuit topologies in a switching period, where the first and third are the same. Hence, the state equation of the 3TSI-DR can be expressed as

$$\dot{\mathbf{x}}(t) = \begin{cases} \mathbf{A}_n\mathbf{x}(t) + \mathbf{B}_1, nT_s < t < (n+d_{n1})T_s \\ \mathbf{A}_n\mathbf{x}(t) + \mathbf{B}_2, (n+d_{n1})T_s < t < (n+d_{n2})T_s \\ \mathbf{A}_n\mathbf{x}(t) + \mathbf{B}_3, (n+d_{n2})T_s < t < (n+1)T_s \end{cases} \tag{27}$$

$$\begin{aligned} \mathbf{x}(t) &= [x_1(t), x_2(t), x_3(t), x_4(t), x_5(t)]^{\mathrm{T}} \\ &= [i_{L1}, i_{L2}, v_0, v_{\mathrm{diff}}, v_{\mathrm{con}}]^{\mathrm{T}} \end{aligned} \tag{28}$$

$$\begin{aligned} \mathbf{A}_n &= \begin{bmatrix} \frac{\partial i'_{L1}}{\partial i_{L1}} & \frac{\partial i'_{L1}}{\partial i_{L2}} & \frac{\partial i'_{L1}}{\partial v_0} & \frac{\partial i'_{L1}}{\partial v_{\mathrm{diff}}} & \frac{\partial i'_{L1}}{\partial v_{\mathrm{con}}} \\ \frac{\partial i'_{L2}}{\partial i_{L1}} & \frac{\partial i'_{L2}}{\partial i_{L2}} & \frac{\partial i'_{L2}}{\partial v_0} & \frac{\partial i'_{L2}}{\partial v_{\mathrm{diff}}} & \frac{\partial i'_{L2}}{\partial v_{\mathrm{con}}} \\ \frac{\partial v'_0}{\partial i_{L1}} & \frac{\partial v'_0}{\partial i_{L2}} & \frac{\partial v'_0}{\partial v_0} & \frac{\partial v'_0}{\partial v_{\mathrm{diff}}} & \frac{\partial v'_0}{\partial v_{\mathrm{con}}} \\ \frac{\partial v'_{\mathrm{diff}}}{\partial i_{L1}} & \frac{\partial v'_{\mathrm{diff}}}{\partial i_{L2}} & \frac{\partial v'_{\mathrm{diff}}}{\partial v_0} & \frac{\partial v'_{\mathrm{diff}}}{\partial v_{\mathrm{diff}}} & \frac{\partial v'_{\mathrm{diff}}}{\partial v_{\mathrm{con}}} \\ \frac{\partial v'_{\mathrm{con}}}{\partial i_{L1}} & \frac{\partial v'_{\mathrm{con}}}{\partial i_{L2}} & \frac{\partial v'_{\mathrm{con}}}{\partial v_0} & \frac{\partial v'_{\mathrm{con}}}{\partial v_{\mathrm{diff}}} & \frac{\partial v'_{\mathrm{con}}}{\partial v_{\mathrm{con}}} \end{bmatrix} \\ &= \begin{bmatrix} 0 & 0 & -\frac{1}{L_1} & 0 & 0 \\ 0 & -\frac{\rho R+1}{\rho L_2} & \frac{\tanh(\rho v_0)}{L_2} & 0 & 0 \\ \frac{1}{C_0} & -\frac{\tanh(\rho v_0)}{C_0} & A_{33} & 0 & 0 \\ -\frac{2}{C_{\mathrm{dc}}} & 0 & 0 & 0 & 0 \\ -\frac{2k_pk_{\mathrm{dc}}}{C_{\mathrm{dc}}} - \frac{k_pk_0}{C_0} & \frac{k_pk_0\tanh(\rho v_0)}{C_0} & A_{53} & k_ik_{\mathrm{dc}} & 0 \end{bmatrix} \end{aligned} \tag{29}$$

$$\mathbf{B}_1 = \begin{bmatrix} \frac{E}{2L_1} \\ 0 \\ 0 \\ 0 \\ g(t) \end{bmatrix}, \mathbf{B}_2 = \begin{bmatrix} 0 \\ 0 \\ 0 \\ 0 \\ g(t) \end{bmatrix}, \text{and } \mathbf{B}_3 = \mathbf{B}_1 \tag{30}$$

where

$$A_{33} = -\frac{\rho(i_{L2} + 2I_s)(1 - \tanh^2(\rho v_0))}{C_0}$$

$$A_{53} = \frac{\rho k_p k_0 (i_{L2} + 2I_s)(1 - \tanh^2(\rho v_0))}{C_0} - k_i k_0$$

$$g(t) = k_p\omega V_{\mathrm{ref}}\cos(\omega t) + k_i V_{\mathrm{ref}}\sin(\omega t)$$

and $\mathbf{x}(t)$ are the state variables; $\mathbf{A}_n$ is the coefficient matrix; $\mathbf{B}_1$, $\mathbf{B}_2$, and $\mathbf{B}_3$ are the input vectors. According to (23) and defining $()' = d()/dt$ as the first derivative of the state variables with respect to time; $\mathbf{A}_n$, $\mathbf{B}_1$, $\mathbf{B}_2$, and $\mathbf{B}_3$ can be calculated,

therein the coefficient matrix $\mathbf{A}_n$ is nonreversible and periodic time-varying.

Therefore, for the 3TSI-DR, $(n+d_{n1})T_s$ and $(n+d_{n2})T_s$ are two transition moments of the state equation in the switching period $[nT_s, (n+1)T_s]$. The 3TSI-DR is continuous smooth within each subpart, but is not differentiable at the transition moments both $(n+d_{n1})T_s$ and $(n+d_{n2})T_s$. That is, the 3TSI-DR is a piecewise smooth periodic time-varying system and belongs to Filippov system. Besides, the coefficient matrix in state equation of the 3TSI-DR is nonreversible and periodic time-varying. As a result, the state equation (27) can be solved by using piecewise integral in the time range from $nT_s$ to $(n+1)T_s$, and the discrete-time mapping model of the 3TSI-DR can be established as

$$\begin{aligned}\mathbf{x}_{n+1} = {} & e^{\mathbf{A}_n T_s}\mathbf{x}_n + e^{\mathbf{A}_n(1-d_{n1})T_s}\int_{nT_s}^{(n+d_{n1})T_s} \\ & \times e^{\mathbf{A}_n((n+d_{n1})T_s-\tau)}\mathbf{B}_1(\tau)\mathrm{d}\tau \\ & + e^{\mathbf{A}_n(1-d_{n2})T_s}\int_{(n+d_{n1})T_s}^{(n+d_{n2})T_s} e^{\mathbf{A}_n((n+d_{n2})T_s-\tau)}\mathbf{B}_2(\tau)\mathrm{d}\tau \\ & + \int_{(n+d_{n2})T_s}^{(n+1)T_s} e^{\mathbf{A}_n((n+1)T_s-\tau)}\mathbf{B}_3(\tau)\mathrm{d}\tau. \end{aligned} \tag{31}$$

Also, the two transition conditions of the 3TSI-DR in the switching period $[nT_s, (n+1)T_s]$ are

$$h_{dn1}(\mathbf{x}(t), t) = x_5(t) - \left(2V_{\text{tri}}\frac{t-nT_s}{T_s}\right) = 0 \tag{32}$$

and

$$h_{dn2}(\mathbf{x}(t), t) = x_5(t) - \left(2V_{\text{tri}}\frac{((n+1)T_s - t)}{T_s}\right) = 0. \tag{33}$$

### C. Mechanism of Fast-Scale Instability

From foregoing analyses, the 3TSI-DR belongs to Filippov system, thereby the saltation matrix can be used to connect adjacent substate transition matrixes of the 3TSI-DR to obtain monodromy matrix in the whole switching period. The eigenvalues of the monodromy matrix are Floquet multipliers. Then, based on Floquet theory, the trajectories of the Floquet multipliers in the complex plane can be used to reveal the mechanism of the fast-scale instability appearing in the 3TSI-DR.

Since the 3TSI-DR is a periodic system, when a small disturbance quantity $\Delta\mathbf{x}(t_0)$ is imposed on its initial state $\mathbf{x}(t_0)$, one can get

$$\Delta\dot{\mathbf{x}}(t) = \mathbf{A}_n\Delta\mathbf{x}(t). \tag{34}$$

The relation between disturbance quantity $\Delta\mathbf{x}(t)$ at any time $t$ and disturbance quantity $\Delta\mathbf{x}(t_0)$ at the initial time $t_0$ is given as

$$\Delta\mathbf{x}(t) = \mathbf{\Phi}\Delta\mathbf{x}(t_0) \tag{35}$$

where $\mathbf{\Phi}$ is the state transition matrix. When $t-t_0 = T_s$, this state transition matrix is regarded as the monodromy matrix of the 3TSI-DR, and the eigenvalues of the monodromy matrix are Floquet multipliers. If all Floquet multipliers are inside the unit circle centered at the origin of the complex plane, the disturbance will disappear over the time and the 3TSI-DR will return to the stable state. If at least one Floquet multiplier goes out of the unit circle, the 3TSI-DR will be in an unstable state, and the instability mechanism can be judged by the trajectories that the Floquet multipliers go out of the unit circle [12].

According to the work in [43], for a Filippov system, there are $N$ continuous smooth subsystems and $N-1$ transition moments, i.e., its state variables are derivable within each time interval $[t_{i-1}, t_i]$ $(i = 1, 2, \ldots, N-1)$. Then, the state transition matrix of each subinterval can be obtained by calculating the following:

$$\mathbf{\Phi}_i = e^{\mathbf{A}_i(t_i - t_{i-1})} \tag{36}$$

where $\mathbf{A}_i$ is the coefficient matrix in the time interval $[t_{i-1}, t_i]$ $(i = 1, 2, \ldots, N-1)$. Therefore, from (36), for the 3TSI-DR in the switching period $[nT_s, (n+1)T_s]$, the substate transition matrixes of its three subintervals can be obtained as

$$\mathbf{\Phi}_{n1} = e^{\mathbf{A}_n(d_{n1}T_s)}, nT_s < t < (n+d_{n1})T_s \tag{37}$$

$$\mathbf{\Phi}_{n2} = e^{\mathbf{A}_n(d_{n2}-d_{n1})T_s}, (n+d_{n1})T_s < t < (n+d_{n2})T_s \tag{38}$$

$$\mathbf{\Phi}_{n3} = e^{\mathbf{A}_n(1-d_{n2})T_s}, (n+d_{n2})T_s < t < (n+1)T_s. \tag{39}$$

For the Filippov system at transition moments, the adjacent substate transition matrixes can be connected by a saltation matrix, and the saltation matrix can be obtained via solving the following:

$$\mathbf{G}_i = \mathbf{I} + \frac{(\mathbf{f}_{i+} - \mathbf{f}_{i-})\mathbf{p}_i^{\mathrm{T}}}{\mathbf{p}_i^{\mathrm{T}}\mathbf{f}_{i-} + \left.\frac{\partial h_i(\mathbf{x}(t),t)}{\partial t}\right|_{t=t_i}} \tag{40}$$

where $\mathbf{f}_{i-}(\mathbf{f}_{i+})$ is the value of the state equation before (after) the time $t_i$, and $\mathbf{p}_i$ is the normal vector of the transition condition $h_i(\mathbf{x}(t),t) = 0$.

According to (31), (32), (33), and (40), the saltation matrixes of the 3TSI-DR at two transition conditions in the switching period $[nT_s, (n+1)T_s]$ can be calculated. When the 3TSI-DR is under the first transition condition, the value of the state equation before the moment $(n+d_{n1})T_s$ is

$$\mathbf{f}_{dn1-} = \mathbf{A}_n\mathbf{x}(nT_s + d_{n1}T_s) + \mathbf{B}_1 = \begin{bmatrix} \frac{E-2x_3(nT_s+d_{n1}T_s)}{2L_1} \\ f_{dn12} \\ f_{dn13} \\ f_{dn14} \\ f_{dn15} \end{bmatrix}. \tag{41}$$

When the 3TSI-DR is under the first transition condition in the switching period $[nT_s, (n+1)T_s]$, the value of the state equation after the moment $(n+d_{n1})T_s$ is

$$\mathbf{f}_{dn1+} = \mathbf{A}_n\mathbf{x}(nT_s + d_{n1}T_s) + \mathbf{B}_2 = \begin{bmatrix} -\frac{x_3(nT_s+d_{n1}T_s)}{L_1} \\ f_{dn12} \\ f_{dn13} \\ f_{dn14} \\ f_{dn15} \end{bmatrix} \tag{42}$$

where

$$\begin{aligned}
f_{dn12} =& -\frac{(\rho R+1)x_2(nT_s+d_{n1}T_s)}{\rho L_2} \\
&+\frac{\tanh(\rho v_0)x_3(nT_s+d_{n1}T_s)}{L_2} \\
f_{dn13} =& \frac{x_1(nT_s+d_{n1}T_s)-\tanh(\rho v_0)x_2(nT_s+d_{n1}T_s)}{C_0} \\
&-\frac{\rho(i_{L2}+2I_s)(1-\tanh^2(\rho v_0))x_3(nT_s+d_{n1}T_s)}{C_0} \\
f_{dn14} =& -\frac{2x_1(nT_s+d_{n1}T_s)}{C_{\text{dc}}} \\
f_{dn15} =& -\frac{2k_pk_{\text{dc}}x_1(nT_s+d_{n1}T_s)}{C_{\text{dc}}}-\frac{k_pk_0x_1(nT_s+d_{n1}T_s)}{C_0} \\
&+\frac{k_pk_0\tanh(\rho v_0)x_2(nT_s+d_{n1}T_s)}{C_0} \\
&+\frac{\rho k_pk_0(i_{L2}+2I_s)(1-\tanh^2(\rho v_0))x_3(nT_s+d_{n1}T_s)}{C_0} \\
&-k_ik_0x_3(nT_s+d_{n1}T_s)+k_ik_{\text{dc}}x_4(nT_s+d_{n1}T_s) \\
&+k_p\omega V_{\text{ref}}\cos(\omega(nT_s+d_{n1}T_s)) \\
&+k_iV_{\text{ref}}\sin(\omega(nT_s+d_{n1}T_s)).
\end{aligned}$$

Also, at the moment $(n+d_{n1})T_s$, the normal vector of the transition condition $h_{dn1}(\mathbf{x}(t),t)=0$ is

$$\mathbf{p}_{dn1}=\nabla h_{dn1}(\mathbf{x}(t),t)=\begin{bmatrix}\frac{\partial h_{dn1}(\mathbf{x}(t),t)}{\partial x_1(t)}\\ \frac{\partial h_{dn1}(\mathbf{x}(t),t)}{\partial x_2(t)}\\ \frac{\partial h_{dn1}(\mathbf{x}(t),t)}{\partial x_3(t)}\\ \frac{\partial h_{dn1}(\mathbf{x}(t),t)}{\partial x_4(t)}\\ \frac{\partial h_{dn1}(\mathbf{x}(t),t)}{\partial x_5(t)}\end{bmatrix}=\begin{bmatrix}0\\0\\0\\0\\1\end{bmatrix} \tag{43}$$

$$\frac{\partial h_{dn1}(\mathbf{x}(t),t)}{\partial t}=\frac{\partial(x_5(t)-(2V_{\text{tri}}\frac{t-nT_s}{T_s}))}{\partial t}=-\frac{2V_{\text{tri}}}{T_s}. \tag{44}$$

In the switching period $[nT_s, (n+1)T_s]$, the saltation matrix of the 3TSI-DR under the first transition condition is given as

$$\begin{aligned}
\mathbf{G}_{dn1}&=\mathbf{I}+\frac{(\mathbf{f}_{dn1+}-\mathbf{f}_{dn1-})\mathbf{p}_{dn1}^{\text{T}}}{\mathbf{p}_{dn1}^{\text{T}}\mathbf{f}_{dn1-}+\frac{\partial h_{dn1}(\mathbf{x}(t),t)}{\partial t}\Big|_{t=nT_s+d_{n1}T_s}} \\
&=\begin{bmatrix}1&0&0&0&\frac{-E}{2L_1(f_{dn15}-\frac{2V_{\text{tri}}}{T_s})}\\0&1&0&0&0\\0&0&1&0&0\\0&0&0&1&0\\0&0&0&0&1\end{bmatrix}.
\end{aligned} \tag{45}$$

When the 3TSI-DR is under the second transition condition in the switching period $[nT_s, (n+1)T_s]$, the value of the state equation before the moment $(n+d_{n2})T_s$ can be got as

$$\mathbf{f}_{dn2-}=\mathbf{A}_n\mathbf{x}(nT_s+d_{n2}T_s)+\mathbf{B}_2=\begin{bmatrix}-\frac{x_3(nT_s+d_{n2}T_s)}{L_1}\\ f_{dn22}\\ f_{dn23}\\ f_{dn24}\\ f_{dn25}\end{bmatrix} \tag{46}$$

and the value of the state equation after the moment $(n+d_{n2})T_s$ is

$$\mathbf{f}_{dn2+}=\mathbf{A}_n\mathbf{x}(nT_s+d_{n2}T_s)+\mathbf{B}_3=\begin{bmatrix}\frac{E-2x_3(nT_s+d_{n2}T_s)}{2L_1}\\ f_{dn22}\\ f_{dn23}\\ f_{dn24}\\ f_{dn25}\end{bmatrix} \tag{47}$$

where

$$\begin{aligned}
f_{dn22} =& -\frac{(\rho R+1)x_2(nT_s+d_{n2}T_s)}{\rho L_2} \\
&+\frac{\tanh(\rho v_0)x_3(nT_s+d_{n2}T_s)}{L_2} \\
f_{dn23} =& \frac{x_1(nT_s+d_{n2}T_s)-\tanh(\rho v_0)x_2(nT_s+d_{n2}T_s)}{C_0} \\
&-\frac{\rho(i_{L2}+2I_s)(1-\tanh^2(\rho v_0))x_3(nT_s+d_{n2}T_s)}{C_0} \\
f_{dn24} =& -\frac{2x_1(nT_s+d_{n2}T_s)}{C_{\text{dc}}} \\
f_{dn25} =& -\frac{2k_pk_{\text{dc}}x_1(nT_s+d_{n2}T_s)}{C_{\text{dc}}}-\frac{k_pk_0x_1(nT_s+d_{n2}T_s)}{C_0} \\
&+\frac{k_pk_0\tanh(\rho v_0)x_2(nT_s+d_{n2}T_s)}{C_0} \\
&+\frac{\rho k_pk_0(i_{L2}+2I_s)(1-\tanh^2(\rho v_0))x_3(nT_s+d_{n2}T_s)}{C_0} \\
&-k_ik_0x_3(nT_s+d_{n2}T_s)+k_ik_{\text{dc}}x_4(nT_s+d_{n2}T_s) \\
&+k_p\omega V_{\text{ref}}\cos(\omega(nT_s+d_{n2}T_s)) \\
&+k_iV_{\text{ref}}\sin(\omega(nT_s+d_{n2}T_s)).
\end{aligned}$$

Also, at the moment $(n+d_{n2})T_s$, the normal vector of the transition condition $h_{dn2}(\mathbf{x}(t),t)=0$ is

$$\mathbf{p}_{dn2}=\nabla h_{dn2}(\mathbf{x}(t),t)=\begin{bmatrix}\frac{\partial h_{dn2}(\mathbf{x}(t),t)}{\partial x_1(t)}\\ \frac{\partial h_{dn2}(\mathbf{x}(t),t)}{\partial x_2(t)}\\ \frac{\partial h_{dn2}(\mathbf{x}(t),t)}{\partial x_3(t)}\\ \frac{\partial h_{dn2}(\mathbf{x}(t),t)}{\partial x_4(t)}\\ \frac{\partial h_{dn2}(\mathbf{x}(t),t)}{\partial x_5(t)}\end{bmatrix}=\begin{bmatrix}0\\0\\0\\0\\1\end{bmatrix} \tag{48}$$

$$\frac{\partial h_{dn2}(\mathbf{x}(t),t)}{\partial t}=\frac{\partial(x_5(t)-(2V_{\text{tri}}\frac{((n+1)T_s-t)}{T_s}))}{\partial t}=\frac{2V_{\text{tri}}}{T_s}. \tag{49}$$

TABLE II
FLOQUET MULTIPLIERS $\lambda_i$ AS $k_p$ CHANGES FROM 13.4 TO 14.3

| $k_p$ | $\lambda_1$ | $\lambda_2$ | $\lambda_3$ | $\lambda_4$ | $\lambda_5$ | State |
|---|---|---|---|---|---|---|
| 13.4 | −0.88302697+0.46530516i | −0.88302697−0.46530516i | 0.76193982 | 0.98897640 | 0.99812011 | Stable |
| 13.5 | −0.90019090+0.43123927i | −0.90019090−0.43123927i | 0.76188579 | 0.98896733 | 0.99813440 | Stable |
| 13.6 | −0.91757477+0.39297930i | −0.91757477−0.39297930i | 0.76183205 | 0.98895836 | 0.99814848 | Stable |
| 13.7 | −0.93518479+0.34909971i | −0.93518479−0.34909971i | 0.76177858 | 0.98894946 | 0.99816234 | Stable |
| 13.8 | −0.95302689+0.29706183i | −0.95302689−0.29706183i | 0.76172537 | 0.98894065 | 0.99817599 | Stable |
| 13.9 | −0.97110766+0.23134493i | −0.97110766−0.23134493i | 0.76167243 | 0.98893192 | 0.99818944 | Stable |
| 14.0 | −0.98943353+0.13287672i | −0.98943353−0.13287672i | 0.76161975 | 0.98892327 | 0.99820269 | Stable |
| 14.1 | −1.14725144 | −0.86877131 | 0.76156731 | 0.98891470 | 0.99821574 | Period-doubling bifurcation |
| 14.2 | −1.26696019 | −0.78673595 | 0.76151511 | 0.98890620 | 0.99822861 | Unstable |
| 14.3 | −1.35769670 | −0.73420444 | 0.76146314 | 0.98889777 | 0.99824128 | Unstable |

In the switching period $[nT_s, (n+1)T_s]$, the saltation matrix of the 3TSI-DR under the second transition condition is got as

$$\mathbf{G}_{dn2} = \mathbf{I} + \frac{(\mathbf{f}_{dn2+} - \mathbf{f}_{dn2-})\mathbf{p}_{dn2}^{\mathrm{T}}}{\mathbf{p}_{dn2}^{\mathrm{T}}\mathbf{f}_{dn2-} + \left.\frac{\partial h_{dn2}(\mathbf{x}(t),t)}{\partial t}\right|_{t=nT_s+d_{n2}T_s}} = \begin{bmatrix} 1 & 0 & 0 & 0 & \frac{E}{2L_1(f_{dn25}+\frac{2V_{\mathrm{ini}}}{T_s})} \\ 0 & 1 & 0 & 0 & 0 \\ 0 & 0 & 1 & 0 & 0 \\ 0 & 0 & 0 & 1 & 0 \\ 0 & 0 & 0 & 0 & 1 \end{bmatrix}. \tag{50}$$

Via combining (37)–(39), (45), and (50), the monodromy matrix of the 3TSI-DR in switching period $[nT_s, (n+1)T_s]$ is calculated as follows:

$$\mathbf{\Phi}_{\mathrm{cycle}} = \mathbf{\Phi}_{n3}\mathbf{G}_{dn2}\mathbf{\Phi}_{n2}\mathbf{G}_{dn1}\mathbf{\Phi}_{n1}. \tag{51}$$

The eigenvalues of the monodromy matrix $\mathbf{\Phi}_{\mathrm{cycle}}$ are the Floquet multipliers $\lambda_i$, thereby $\lambda_i$ can be obtained by solving $|\lambda_i\mathbf{I}-\mathbf{\Phi}_{\mathrm{cycle}}| = 0$. According to aforementioned introduction, the flowchart, regarding the judgment methodology about the instability mechanism of the piecewise nonlinear smooth periodic time-varying system, is drawn in Fig. 10. In the following, the values of the circuit parameters, as listed in Table I, are substituted into each step mentioned in Fig. 10, so as to calculate the various Floquet multipliers when the proportion parameter $k_p$ is increasing. As $k_p$ changes from 13.4 to 14.3, via adopting eig function in MATLAB software, the Floquet multipliers are calculated, as given in Table II. Also, the changing trajectories of the Floquet multipliers are depicted in Fig. 11. Obviously, from Fig. 11(a), all the Floquet multipliers keep inside the unit circle when $k_p<14.1$, that is the 3TSI-DR stays in the stable state. However, when $k_p\geq 14.1$, the Floquet multiplier $\lambda_1$ goes out of the unit circle along the negative real axis, as shown in Fig. 11(b), but the rest Floquet multipliers $\lambda_2$, $\lambda_3$, $\lambda_4$, and $\lambda_5$ are still inside of the unit circle. That is, at this time, the 3TSI-DR is in an unstable state, and the instability mechanism can be judged by the trajectory that the Floquet multiplier $\lambda_1$ moves out of the unit circle. Based on Floquet theory, which has been described in Fig. 10, it can be revealed from Table II and Fig. 11 that the mechanism of the fast-scale instability in the 3TSI-DR is caused by the occurrence of the period-doubling bifurcation as the increase of $k_p$. When the period-doubling bifurcation occurs, the operation period of the 3TSI-DR is going to become an integer multiple of the switching period.

Specially, the simulation results in Section II-B have shown that the full-bifurcation instability occurs in the 3TSI-DR with respect to $k_p = 16$, where the 3TSI-DR loses the period-1 mode in the whole line period and the operation period changes from period-2 to period-4. Here, with $k_p$ changing from 14.4 to 16.2, various Floquet multipliers are calculated in Table III, and the changing trajectories are displayed in Fig. 12. It is obvious from Fig. 12 that the Floquet multiplier $\lambda_1$ goes away from the unit circle along the negative real axis while the rest stay inside of the unit circle. Hence, the instability phenomenon that the oscillation period of the 3TSI-DR changes from period-2 to period-4 is also the period-doubling bifurcation when the period-2 is considered as the fundamental frequency. That is, the dynamical essence of the full-bifurcation instability is the developed period-doubling bifurcation.

### D. Floquet Multiplier Sensitivity

In practical engineering, the key parameters affecting the stability of the system are concerned by electrical engineers. The sensitivity analysis of the circuit parameters, as an effective method to recognize the key parameters of the nonlinear system, can be used to identify the key parameters affecting the stability of the 3TSI-DR. According to the work in [13], for the 3TSI-DR, the Floquet multiplier sensitivities of the different circuit parameters based on normalization can be calculated as follows:

$$\left|\left.\frac{\partial\lambda_i/\lambda_i}{\partial\sigma/\sigma}\right|_{\sigma_0}\right| = \left|\frac{H_i^{\mathrm{T}}\left(\frac{\partial\mathbf{\Phi}_{\mathrm{cycle}}(\sigma)}{\partial\sigma}\times\frac{\sigma}{\mathbf{\Phi}_{\mathrm{cycle}}(\sigma)}\right)\Big|_{\sigma_0}Q_i}{H_i^{\mathrm{T}}Q_i}\right|. \tag{52}$$

In (52), the monodromy matrix $\mathbf{\Phi}_{\mathrm{cycle}}(\sigma)$ is the function of circuit parameters $\sigma$, $H_i{}^{\mathrm{T}}$ is the left eigenvector related to Floquet multiplier $\lambda_i$, and $Q_i$ is the right eigenvector related to Floquet multiplier $\lambda_i$. For the 3TSI-DR, there is $\sigma = (C_0, f_s, k_p, L_1, L_2, R, k_i)$. By substituting (51) into (52), the module values about the normalized first-order Floquet multiplier sensitivities of the different circuit parameters can be obtained and summarized in Table IV. From Table IV, these normalized Floquet multiplier sensitivities are used to describe the movement of the Floquet multiplier $\lambda_i$ in the unit circle when a small disturbance is added on the circuit parameter $\sigma_0$.

TABLE III
FLOQUET MULTIPLIERS $\lambda_i$ AS $k_p$ CHANGES FROM 14.4 TO 16.2

| $k_p$ | $\lambda_1$ | $\lambda_2$ | $\lambda_3$ | $\lambda_4$ | $\lambda_5$ | State |
|---|---|---|---|---|---|---|
| 14.4 | −1.43684942 | −0.69380309 | 0.76141141 | 0.98888942 | 0.99825378 | Unstable |
| 14.6 | −1.57805252 | −0.63180237 | 0.76130861 | 0.98887291 | 0.99827824 | Unstable |
| 14.8 | −1.70742375 | −0.58400465 | 0.76120668 | 0.98885666 | 0.99830202 | Unstable |
| 15.0 | −1.83078421 | −0.54472224 | 0.76110555 | 0.98884067 | 0.99832514 | Unstable |
| 15.2 | −1.95101071 | −0.51121900 | 0.76100522 | 0.98882491 | 0.99834763 | Unstable |
| 15.4 | −2.06981171 | −0.48193661 | 0.76090563 | 0.98880938 | 0.99836953 | Unstable |
| 15.6 | −2.18832996 | −0.45589185 | 0.76080676 | 0.98879406 | 0.99839084 | Unstable |
| 15.8 | −2.30740208 | −0.43241923 | 0.76070858 | 0.98877895 | 0.99841160 | Unstable |
| 16.0 | −2.42768229 | −0.41104545 | 0.76061108 | 0.98876404 | 0.99843183 | Unstable |
| 16.2 | −2.54971642 | −0.39142000 | 0.76051421 | 0.98874932 | 0.99845154 | Unstable |

TABLE IV
FIRST-ORDER FLOQUET MULTIPLIER SENSITIVITIES OF DIFFERENT CIRCUIT PARAMETERS BASED ON NORMALIZATION

| Circuit Parameters | $\left\lvert\frac{\partial\lambda_{1,2}/\lambda_{1,2}}{\partial\sigma/\sigma}\right\rvert$ | $\left\lvert\frac{\partial\lambda_3/\lambda_3}{\partial\sigma/\sigma}\right\rvert$ | $\left\lvert\frac{\partial\lambda_4/\lambda_4}{\partial\sigma/\sigma}\right\rvert$ | $\left\lvert\frac{\partial\lambda_5/\lambda_5}{\partial\sigma/\sigma}\right\rvert$ |
|---|---|---|---|---|
| $C_0$=68μF | 6514.05131615 | 4337.17600179 | 179.44676415 | 28.85939319 |
| $f_s$=8kHz | 6376.80388359 | 5839.56096737 | 1486.00598904 | 205.29888331 |
| $k_p$=13.4 | 6209.98271709 | 5254.79139128 | 1823.55926693 | 1809.33930851 |
| $L_1$=1mH | 3060.88620597 | 551.52093070 | 708.96447177 | 119.09516213 |
| $L_2$=2mH | 474.13264182 | 609.98040749 | 711.78892848 | 69.95724560 |
| $R$=4.5Ω | 428.43806898 | 506.41142134 | 594.74766047 | 58.35790568 |
| $k_i$=200 | 6.11863380 | 5.49876526 | 188.72168166 | 186.62358613 |

Also, the comparison on the normalized Floquet multiplier sensitivities of the different circuit parameters is displayed in Fig. 13. Fig. 13 shows that $\lambda_{1,2}$ are greatly sensitive to circuit parameters $C_0$, $f_s$, $k_p$, and $L_1$; $\lambda_3$ is greatly sensitive to circuit parameter $C_0$, $f_s$, and $k_p$; $\lambda_4$ is sensitive to circuit parameters $f_s$ and $k_p$; $\lambda_5$ is only sensitive to circuit parameter $k_p$. Obviously, for the 3TSI-DR, the normalized Floquet multiplier sensitivities in response to different circuit parameters are various. Since the period-doubling bifurcation of the 3TSI-DR is mainly related to $\lambda_{1,2}$, by comparison, it can be identified that the main circuit parameters $C_0$ and $L_1$ as well as the control circuit parameters $f_s$ and $k_p$ are the key parameters affecting the stability of the 3TSI-DR. Certainly, these results can offer design-oriented information for the optimization design of the 3TSI-DR to guarantee its stable operation in practice.

## IV. COMPARISONS BETWEEN THEORETICAL ANALYSES AND SIMULATION RESULTS

### A. Unstable Angle Ranges of Fast-Scale Instability

Simulations in Section II-B have shown that the fast-scale instability of the 3TSI-DR appears around the peaks and troughs of the inverter-side ac output voltage, that is at the peaks and troughs of the reference voltage. Via defining that the reference voltage is $v_{\rm ref} = V_{\rm ref}\sin(\theta)$ and considering that the unstable angle range of the fast-scale instability in the 3TSI-DR is within $0<\theta\leq\pi$, under the given circuit parameter conditions listed in Table I, as $k_p$ changes the corresponding monodromy matrix and its Floquet multipliers can be calculated. If one of the Floquet multipliers goes out of the unit circle along the negative real axis (i.e., its value reaches $-1$), the angle range of the fast-scale instability at this time is recorded [11]. By this way, the unstable angle ranges (i.e., from $\theta_1$ to $\theta_2$) of the fast-scale instability in the 3TSI-DR with respect to the changing $k_p$ are shown in Fig. 14. For another, the unstable angle ranges of the fast-scale instability obtained from PSpice simulation are also displayed in Fig. 14 for the purpose of verifying the results from theoretical analyses. Hence, the following results can be drawn from Fig. 14.

The critical point Pc in Fig. 14 corresponds to the critical stable operation parameter condition, and under this parameter condition, the fast-scale instability starts to occur in the 3TSI-DR. Clearly, when $k_p<14.1$, the 3TSI-DR operates stably during the whole line period. But, when $k_p\geq14.1$, the period-doubling bifurcation appears in the 3TSI-DR, and the unstable angle range expands with the proportion parameter $k_p$ increasing. Especially, when $k_p\geq15.8$, the unstable angle range is from 0 to 180°, i.e., at this time the full-bifurcation instability occurs in the 3TSI-DR, which is the developed period-doubling bifurcation.

### B. Stability Boundary

The analysis results on Floquet multiplier sensitivities have explained that different circuit parameters have various effects on the stability of the 3TSI-DR. Here, the stability boundaries of the 3TSI-DR are discussed in various parameter spaces via both theoretical analyses and PSpice simulations, which are formed by a series of critical stable operation parameter conditions. It can be seen from Fig. 15(a)–(c) that the theoretical results agree with simulations. Note that the critical points Pc marked in Fig. 15(a)–(c) represent the same critical stable operation parameter condition, as marked in Fig. 14. Hence, under the stable region parameter conditions in Fig. 15(a)–(c), the 3TSI-DR will operate normally whatever the angle is.

The stability boundaries in the $C_0$-$k_p$ plane with respect to different inverter-side filter inductor $L_1$ are shown in Fig. 15(a). From Fig. 15(a), one can see that when the inverter-side filter

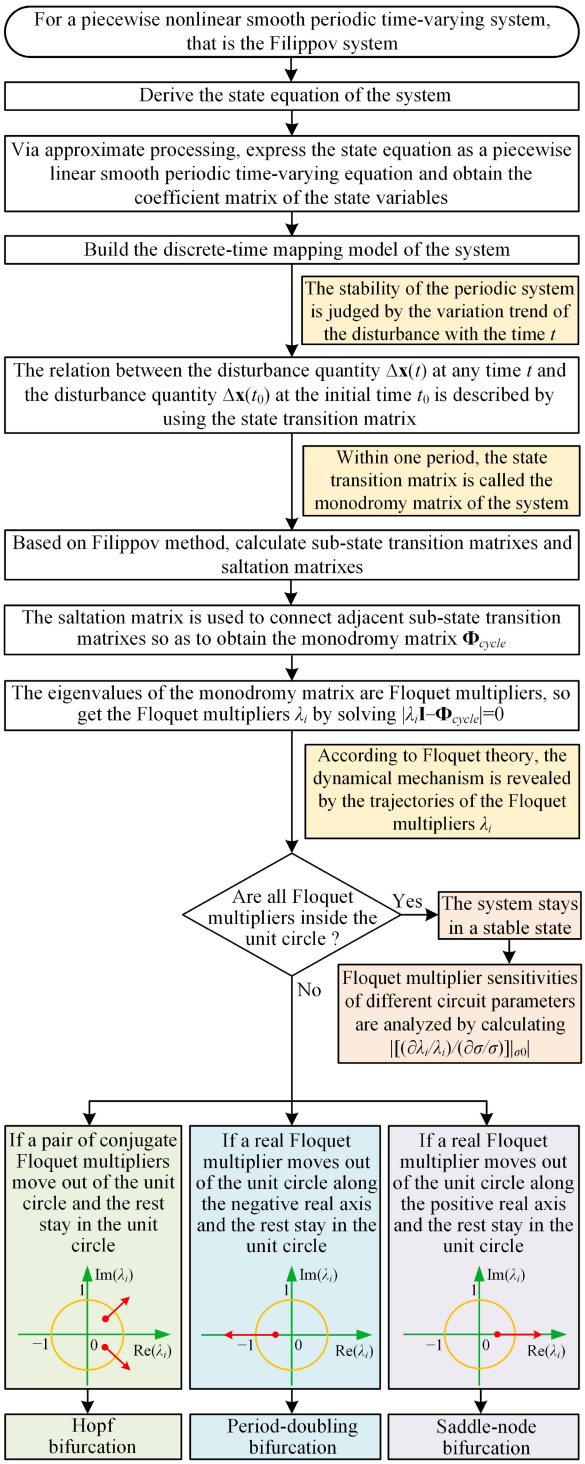


Fig. 10. Flowchart on the theoretical methodology.

capacitor $C_0$ is determined, the stability region of the 3TSI-DR will be reduced as $L_1$ decreases, such as the stability region is $Q_1+Q_2+Q_3$ at $L_1 = 1.2$ mH, but the stability region is reduced to $Q_3$ at $L_1 = 0.8$ mH. Also, when $L_1$ is determined, the stability region of the 3TSI-DR will be reduced as $C_0$ decreases. This indicates that for a particular $L_1$ and $C_0$, the 3TSI-DR is going to be unstable when $L_1$ or $C_0$ is too small. That is, with the decrease

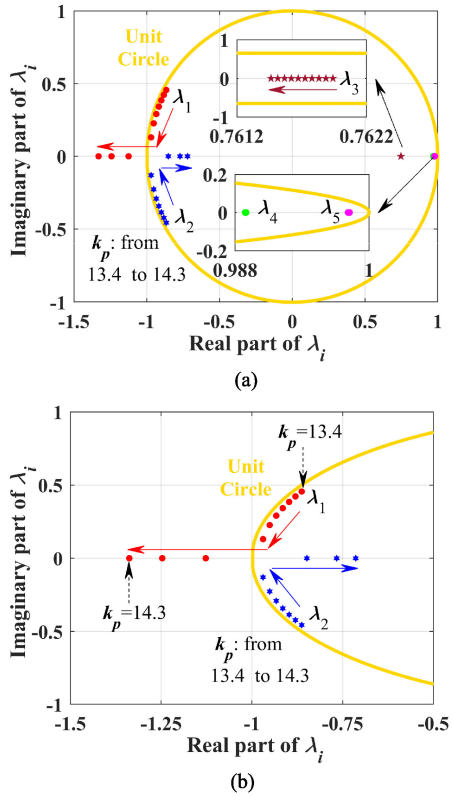


Fig. 11. (a) Trajectories of Floquet multipliers as $k_p$ changes from 13.4 to 14.3. (b) Close-up view.

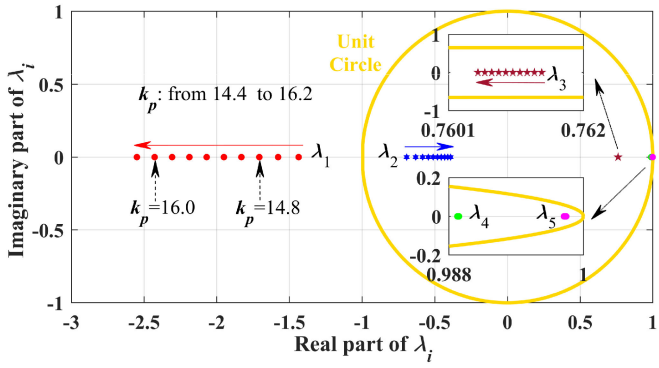


Fig. 12. Trajectories of Floquet multipliers as $k_p$ changes from 14.4 to 16.2.

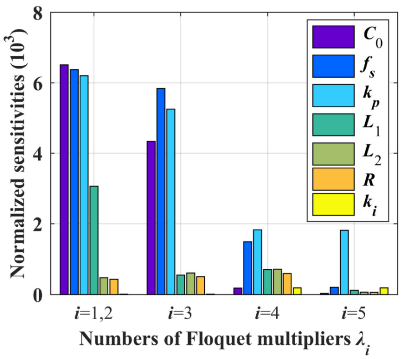


Fig. 13. Normalized Floquet multiplier sensitivities of the different circuit parameters.

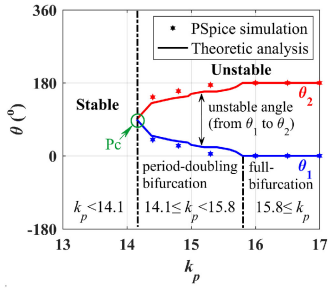


Fig. 14. Unstable angle ranges of the fast-scale instability with $k_p$ changing.

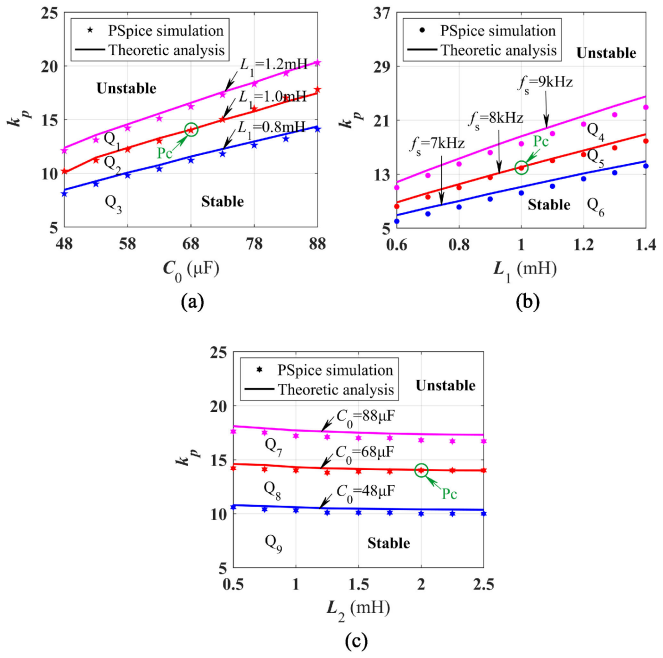


Fig. 15. Stability boundaries of the 3TSI-DR. (a) In the $C_0$-$k_p$ plane. (b) In the $L_1$-$k_p$ plane. (b) In the $L_2$-$k_p$ plane.

of $L_1$ or $C_0$, the 3TSI-DR will lose stability by period-doubling bifurcation.

The stability boundaries in the $L_1$-$k_p$ plane with respect to different switching frequency $f_s$ are shown in Fig. 15(b). We can find that the stability region of the 3TSI-DR is $Q_5$+$Q_6$ when $f_s$ is selected as 8 kHz, and the stability region is reduced to $Q_6$ when $f_s$ is selected as 7 kHz. This suggests that when $f_s$ is too small, the 3TSI-DR will be unstable via period-doubling bifurcation.

The stability boundaries in the $L_2$-$k_p$ plane with respect to different inverter-side filter capacitor $C_0$ are shown in Fig. 15(c), which illustrate that the stability region is $Q_7$+$Q_8$+$Q_9$ at $C_0$ = 88 $\mu$F, and the stability region is reduced to $Q_9$ at $C_0$ = 48 $\mu$F. However, when $C_0$ is determined, the stability boundaries of the 3TSI-DR have not obvious change as $L_2$ increase or decrease.

From the aforementioned analyses, it can be concluded that the stability boundaries of the 3TSI-DR vary significantly in various parameter spaces. The period-doubling bifurcation will occur in the 3TSI-DR if $C_0$, $L_1$, or $f_s$ is too small, that is, appropriately increasing the values of $C_0$, $L_1$, and $f_s$ can enlarge the stability region of the 3TSI-DR. These results can be applied

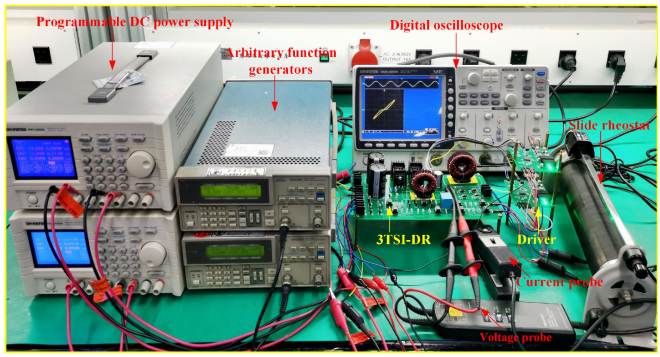


Fig. 16. Experimental platform of the 3TSI-DR.

for the parameter adjustment of the 3TSI-DR to ensure its stable operation in an adequately wide parameter range.

## V. Experimental Verifications

### A. Experimental Platform

An experimental prototype is built to verify the fast-scale instability of the 3TSI-DR, which is shown in Fig. 16. In the experiment, the experimental parameter values are chosen as the same as adopted in both simulations and theoretical analyses. In addition, the power MOSFET IRFP264N are selected as the switches $S_1$, $S_2$, $S_3$, and $S_4$; the standard recovery rectifiers 1N5408 are selected as the diodes $D_1$, $D_2$, $D_3$, and $D_4$; the LF356 is chosen as the operational amplifier; the LM311 is chosen as the comparator. The dual-channel gate driver UCC21520 is used for driving the switches. The voltage transformer HPT205A is used for sampling the inverter-side ac output voltage. The programmable power supply GWINSTEK PST 3202 is used for powering the dc supplies. The arbitrary function generator Tektronix AFG 310 is used for generating the reference voltage signal and the unipolar carrier voltage signal. The differential voltage probe Tektronix P5200A is used to detect the inverter-side ac output voltage $v_0$. The current probes Tektronix A622 are used to detect the inverter-side ac output current $i_{\rm M}$ and the inverter-side filter inductor current $i_{L1}$. Then, the digital oscilloscope GWINSTEK GDS 3254 is used to capture the measured waveforms in the probes.

### B. Experimental Results

Fig. 17 shows the experimental waveforms of the 3TSI-DR under $k_p = 4.4$ (i.e., $R_k = 22$ kΩ). Fig. 17(a) displays the time-domain waveforms of the inverter-side ac output voltage $v_0$ and the inverter-side ac output current $i_{\rm M}$. Fig. 17(b) suggests that the $v_0$-$i_{\rm M}$ curve is a typical pinched hysteresis loop. Besides, the FFT analysis of $v_0$ is shown in Fig. 17(c), and the FFT analysis of $i_{\rm M}$ is shown in Fig. 17(d). We can obtain that the THD of $v_0$ is 2.40% and the THD of $i_{\rm M}$ is 6.81%. Hence, from Fig. 17, the 3TSI-DR under $k_p = 4.4$ can work in a stable state.

Fig. 18 shows the experimental waveforms of the 3TSI-DR under $k_p = 14.8$ (i.e., $R_k = 74$ kΩ). Fig. 18(a) and (b) displays that the 3TSI-DR has experienced obvious oscillations, and the diode-bridge rectifier with inductive load still maintains

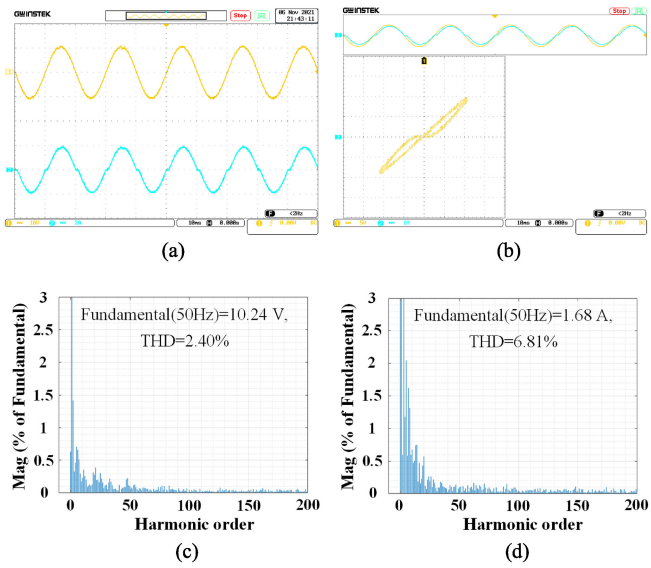


Fig. 17. Experimental results of the 3TSI-DR under $k_p = 4.4$. (a) Time-domain waveforms of the inverter-side ac output voltage $v_0$ and ac output current $i_M$ (upper trace: 10 V/div for $v_0$; lower trace: 2 A/div for $i_M$; time: 10 ms/div). (b) $v_0$-$i_M$ curve (horizontal axis: 5 V/div for $v_0$; vertical axis: 1 A/div for $i_M$). (c) FFT analysis of $v_0$. (d) FFT analysis of $i_M$.

the pinched hysteresis loop but has gone through distortion. The FFT analyses of $v_0$ and $i_M$ are shown in Fig. 18(c) and (d). It is easy found that the THD of $v_0$ increases to 9.84% and the THD of $i_M$ increases to 8.84%, that is, the working environment of the diode-bridge rectifier-based load is going to be bad. Fig. 18(e) displays the experimental waveforms of the inverter-side ac output voltage $v_0$ and the inverter-side filter inductor current $i_{L1}$. Also, the partial enlarged views of Fig. 18(e) are given in Fig. 18(f)–(h), as expected that the fast-scale instability can be observed. Then, the Cursor tool of the digital oscilloscope is employed to measure the operation periods of the experimental waveforms $v_0$ and $i_{L1}$. As displayed in the upper left corner of Fig. 18(f)–(h), the measurement records are the switching period (125 $\mu$s), twice the switching period (250 $\mu$s), and four times the switching period (500 $\mu$s). Hence, the fast-scale instability observed in the 3TSI-DR is the period-doubling oscillation on switching period scale.

Fig. 19 shows the experimental waveforms of the 3TSI-DR under $k_p = 16$ (i.e., $R_k = 80\,\text{k}\Omega$). Fig. 19(a) and (b) indicates that the 3TSI-DR appears more obvious oscillations. At this time, from Fig. 19(c) and (d), the THD of $v_0$ has increased to 12.81% and the THD of $i_M$ has increased to 9.53%. Obviously, the work environment of the diode-bridge rectifier-based load becomes worse as $k_p$ increase. Similarly, the Cursor tool is employed to measure the oscillation periods of the experimental waveforms $v_0$ and $i_{L1}$, as shown in Fig. 19(e)–(g), the measurement records as given in the upper left corner of Fig. 19(f) and (g) are twice the switching period (250 $\mu$s) and four times the switching period (500 $\mu$s). That is, at this time, the 3TSI-DR has lost the period-1 mode in the whole line period and the full-bifurcation instability appears.

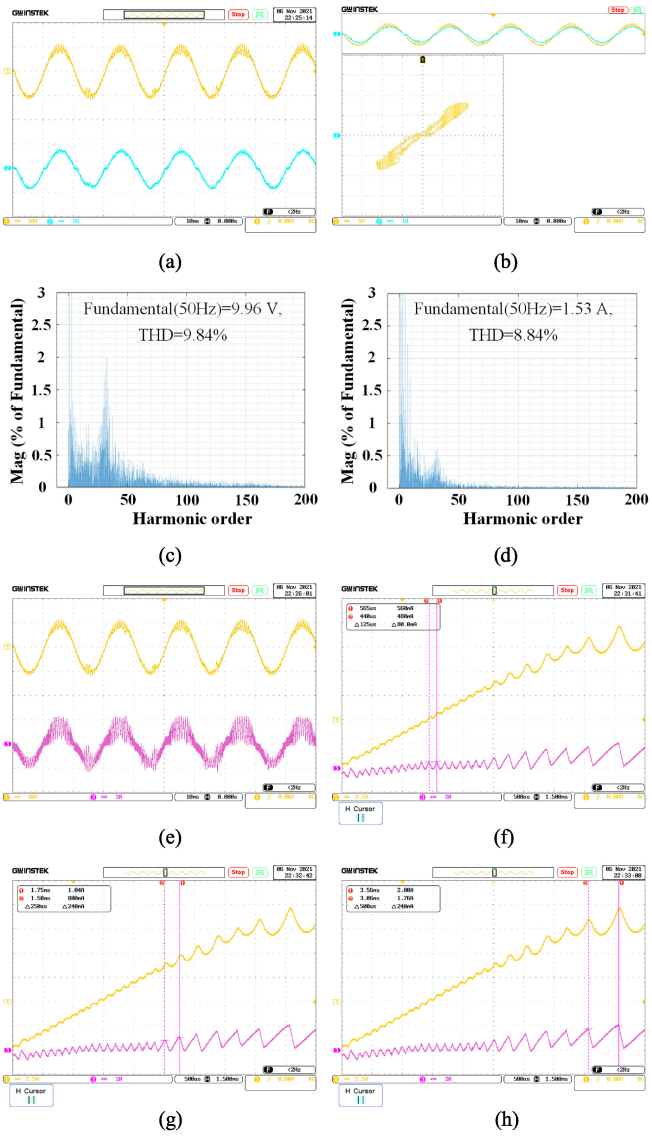


Fig. 18. Experimental results of the 3TSI-DR under $k_p = 14.8$. (a) Time-domain waveforms of the inverter-side ac output voltage $v_0$ and ac output current $i_M$ (upper trace: 10 V/div for $v_0$; lower trace: 2 A/div for $i_M$; time: 10 ms/div). (b) $v_0$-$i_M$ curve (horizontal axis: 5 V/div for $v_0$; vertical axis: 1 A/div for $i_M$). (c) FFT analysis of $v_0$. (d) FFT analysis of $i_M$. (e) Time-domain waveforms of $v_0$ and the inverter-side filter inductor current $i_{L1}$ (upper trace: 10 V/div for $v_0$; lower trace: 2 A/div for $i_{L1}$; time: 10 ms/div). (f)–(h) Close-up view of $v_0$ and $i_{L1}$ (upper trace: 2.5 V/div for $v_0$; lower trace: 2 A/div for $i_{L1}$; time: 500 $\mu$s/div), the measured records are shown in the upper left corner.

### C. Discussion on Experimental Results and Simulation Results

For the 3TSI-DR, when the proportion parameter is successively increased to $k_p = 4.4$, $k_p = 14.8$, and $k_p = 16$, the experimental results have been presented in Figs. 17–19, and the corresponding simulation results are shown in Figs. 4–6. Clearly, the experimental results are almost consistent with the simulation results by comparing Fig. 17 with Fig. 4, Fig. 18 with Fig. 5, and Fig. 19 with Fig. 6, respectively; and minor deviation in details are caused by some inevitable actual factors in the hardware circuit, such as the equivalent series resistances of inductors and capacitors as well as the on-resistance of MOSFET, etc. All in all, the agreement between the experimental results

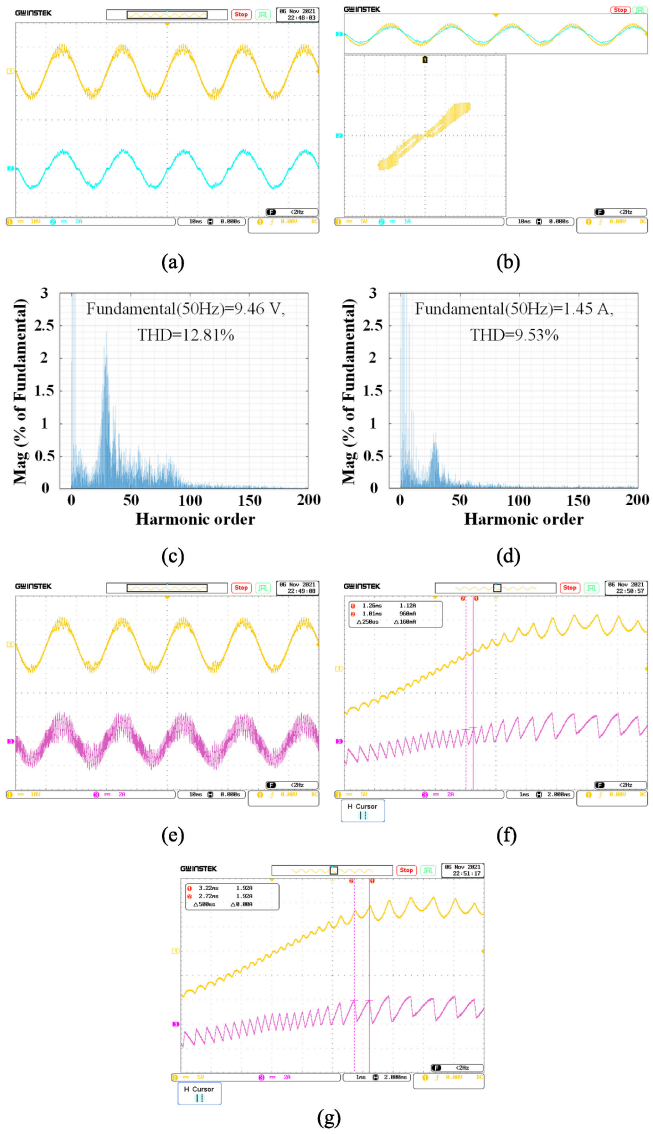


Fig. 19. Experimental results of the 3TSI-DR under $k_p = 16$. (a) Time-domain waveforms of the inverter-side ac output voltage $v_0$ and ac output current $i_{\rm M}$ (upper trace: 10 V/div for $v_0$; lower trace: 2 A/div for $i_{\rm M}$; time: 10 ms/div). (b) $v_0$-$i_{\rm M}$ curve (horizontal axis: 5 V/div for $v_0$; vertical axis: 1 A/div for $i_{\rm M}$). (c) FFT analysis of $v_0$. (d) FFT analysis of $i_{\rm M}$. (e) Time-domain waveforms of $v_0$ and the inverter-side filter inductor current $i_{L1}$ (upper trace: 10 V/div for $v_0$; lower trace: 2 A/div for $i_{L1}$; time: 10 ms/div). (f) and (g) Close-up view of $v_0$ and $i_{L1}$ (upper trace: 5 V/div for $v_0$; lower trace: 2 A/div for $i_{L1}$; time: 1 ms/div), the measured records are shown in the upper left corner.

and simulation results again confirms the theoretical analyses that the occurrence of the period-doubling bifurcation leads to the fast-scale instability breaking out in the 3TSI-DR.

In addition, the following important points can be obtained by contrast the experimental results shown in Figs. 17–19 and the simulation results shown in Figs. 4–6. First, the 3TSI-DR will be subjected to the fast-scale instability on switching period scale in response to improper proportion parameter $k_p$, and the fast-scale instability observed in the 3TSI-DR is caused by period-doubling bifurcation. Second, the 3TSI-DR will lose the period-1 mode in the whole line period when the full-bifurcation instability occurs, and its dynamical essence is the developed period-doubling bifurcation. Third, the fast-scale instability in the 3TSI-DR can increase the harmonic content of the inverter-side ac output voltage $v_0$ and ac output current $i_{\rm M}$, so as to deteriorate the work environment of the diode-bridge rectifier-based nonlinear load and seriously affects the stable operation of the 3TSI-DR.

## VI. Conclusion

The fast-scale instability of the 3TSI-DR has been investigated from PSpice simulations, theoretical analyses, and circuit experiments. Research results show that the fast-scale instability can increase the harmonic content of the 3TSI-DR to affect its stable operation seriously. Consequently, the mechanism of the fast-scale instability discovered in the 3TSI-DR is revealed via combining Filippov method and Floquet theory, which demonstrates that the fast-scale instability of the 3TSI-DR is caused by the occurrence of the period-doubling bifurcation. In addition, the Floquet multiplier sensibilities of the different circuit parameters indicate that the main circuit parameters $C_0$ and $L_1$ as well as the control circuit parameters $f_s$ and $k_p$ are the key parameters affecting the stability of the 3TSI-DR; the unstable angle ranges of the fast-scale instability with circuit parameters changing illustrate that under certain parameter conditions, the 3TSI-DR will lose the period-1 mode in the whole line period and stay at the full-bifurcation instability; the stability boundaries in various parameter spaces suggest that the stability regions of the 3TSI-DR will be reduced with the circuit parameters $C_0$, $L_1$, or $f_s$ decreasing. The conclusions in this article are useful for the optimal design of the 3TSI-DR to avoid the occurrence of the period-doubling bifurcation and to ensure its stable operation in an adequately wide parameter range. Besides, it is expected to provide theoretical guidance for the study on the instability behaviors in the multilevel inverters with nonlinear loads.

## References

[1] S. Peyghami, P. Palensky, and F. Blaabjerg, "An overview on the reliability of modern power electronic based power systems," *IEEE Open J. Power Electron.*, vol. 1, no. 2020, pp. 34–50, Feb. 2020.
[2] C. K. Tse and M. Di Bernardo, "Complex behavior in switching power converters," *Proc. IEEE*, vol. 90, no. 5, pp. 768–781, May 2002.
[3] C. M. F. S. Reza and D. D.-C. Lu, "Recent progress and future research direction of nonlinear dynamics and bifurcation analysis of grid-connected power converter circuits and systems," *IEEE J. Emerg. Sel. Topics Power Electron.*, vol. 8, no. 4, pp. 3193–3203, Dec. 2020.
[4] W. Hu, R. Yang, X. Wang, and F. Zhang, "Stability analysis of voltage controlled buck converter feed from a periodic input," *IEEE Trans. Ind. Electron.*, vol. 68, no. 4, pp. 3079–3089, Apr. 2021.
[5] X. Wang et al., "Impact of controller saturation on instability behavior of grid-connected inverters," *IEEE Trans. Power Electron.*, vol. 37, no. 7, pp. 7739–7750, Jul. 2022.
[6] D. C. Hamill and D. J. Jeffries, "Subharmonics and chaos in a controlled switched-mode power converter," *IEEE Trans. Circuits Syst.*, vol. 35, no. 8, pp. 1059–1061, Aug. 1988.
[7] J. H. B. Deane and D. C. Hamill, "Instability, subharmonics, and chaos in power electronic systems," *IEEE Trans. Power Electron.*, vol. 5, no. 3, pp. 260–268, Jul. 1990.
[8] A. Kavitha and G. Uma, "Experimental verification of Hopf bifurcation in DC-DC Luo converter," *IEEE Trans. Power Electron.*, vol. 23, no. 6, pp. 2878–2883, Nov. 2008.
[9] Z. T. Zhusubaliyev, E. Mosekilde, and O. O. Yanochkina, "Torus-bifurcation mechanisms in a DC/DC converter with pulsewidth-modulated control," *IEEE Trans. Power Electron.*, vol. 26, no. 4, pp. 1270–1279, Apr. 2011.

[10] A. El Aroudi, R. Haroun, M. S. Al-Numay, J. Calvente, and R. Giral, "Fast-scale stability analysis of a DC-DC boost converter with a constant power load," *IEEE J. Emerg. Sel. Topics Power Electron.*, vol. 9, no. 1, pp. 549–558, Feb. 2021.
[11] H. H. C. Iu, Y. F. Zhou, and C. K. Tse, "Fast-scale instability in a PFC boost converter under average current-mode control," *Int. J. Circuit Theory Appl.*, vol. 31, no. 6, pp. 611–624, Nov./Dec. 2003.
[12] F. Wang, H. Zhang, and X. Ma, "Analysis of slow-scale instability in boost PFC converter using the method of harmonic balance and Floquet theory," *IEEE Trans. Circuits Syst. I: Regular Papers*, vol. 57, no. 2, pp. 405–414, Feb. 2010.
[13] H. Zhang, S. Dong, Y. Zhang, and B. He, "Intermediate-frequency oscillation behavior of one-cycle controlled SEPIC power factor correction converter via Floquet multiplier sensitivity analysis," *Int. J. Bifurcation Chaos*, vol. 26, no. 10, Sep. 2016, Art. no. 1650163.
[14] D. P. Shankar, U. Govindarajan, and K. Karunakaran, "Period-bubbling and mode-locking instabilities in a full-bridge DC-AC buck inverter," *IET Power Electron.,* vol. 6, no. 9, pp. 1956–1970, Nov. 2013.
[15] H. Zhang, S. Dong, W. M. Guan, and Y. Liu, "Analysis of fast-scale bifurcation in peak current controlled buck-boost inverter based on unified averaged model," *Int. J. Bifurcation Chaos*, vol. 26, no. 5, May 2016, Art. no. 1650074.
[16] M. S. Manoharan, A. Ahmed, and J.-H. Park, "Modeling and bifurcation analysis for photovoltaic single-sourced trinary inverter with auxiliary floating capacitors controlled by finite-control-set model predictive control," *IEEE J. Emerg. Sel. Topics Power Electron.*, vol. 9, no. 4, pp. 5002–5015, Aug. 2021.
[17] X. M. Wang and B. Zhang, "Study of bifurcation and chaos in single-phase SPWM inverter," *Trans. China Electrotech. Soc.*, vol. 24, no. 1, pp. 101–107, Jan. 2009.
[18] M. Li, D. Dai, and X. K. Ma, "Slow-scale and fast-scale instabilities in voltage-mode controlled full-bridge inverter," *Circuits Syst. Signal Process.*, vol. 27, no. 6, pp. 811–831, Dec. 2008.
[19] H. Y. Ji, F. Xie, L. Shen, R. Yang, and B. Zhang, "Unstable behavior analysis and stabilization of double-loop proportional-integral control H-bridge inverter with inductive impedance load," *Int. J. Circuit Theory Appl.*, vol. 50, no. 3, pp. 904–925, Mar. 2022.
[20] L. H. Yang, L. Yang, F. Yang, and X. K. Ma, "Slow-scale and fast-scale instabilities in parallel-connected single-phase H-bridge inverters: A design-oriented study," *Int. J. Bifurcation Chaos*, vol. 30, no. 1, Jan. 2020, Art. no. 2050005.
[21] A. El Aroudi, E. Rodriguez, M. Orabi, and E. Alarcon, "Modeling of switching frequency instabilities in buck-based DC-AC H-bridge inverters," *Int. J. Circuit Theory Appl.*, vol. 39, no. 2, pp. 175–193, Feb. 2011.
[22] V. Avrutin and Z. Zhusubaliyev, "Piecewise-linear map for studying border collision phenomena in DC/AC converters," *Int. J. Bifurcation Chaos*, vol. 30, no. 7, Jun. 2020, Art. no. 2030015.
[23] X. He, C. He, S. Pan, H. Geng, and F. Liu, "Synchronization instability of inverter-based generation during asymmetrical grid faults," *IEEE Trans. Power Syst.*, vol. 37, no. 2, pp. 1018–1031, Mar. 2022.
[24] J. Rodriguez, S. Bernet, P. K. Steimer, and I. E. Lizama, "A survey on neutral-point-clamped inverters," *IEEE Trans. Ind. Electron.*, vol. 57, no. 7, pp. 2219–2230, Jul. 2010.
[25] Y. Liang, R. Wang, and B. Hu, "Single-switch open-circuit diagnosis method based on average voltage vector for three-level T-type inverter," *IEEE Trans. Power Electron.*, vol. 36, no. 1, pp. 911–921, Jan. 2021.
[26] R. Teichmann and S. Bernet, "A comparison of three-level converters versus two-level converters for low-voltage drives, traction, and utility applications," *IEEE Trans. Ind. Appl.*, vol. 41, no. 3, pp. 855–865, May–Jun. 2005.
[27] M. Lak, Y.-T. Tsai, B.-R. Chuang, T.-L. Lee, and M. H. Moradi, "A hybrid method to eliminate leakage current and balance neutral point voltage for photovoltaic three-level T-type inverter," *IEEE Trans. Power Electron.*, vol. 36, no. 10, pp. 12070–12089, Oct. 2021.
[28] A. Deshpande, Y. Chen, B. Narayanasamy, Z. Yuan, C. Chen, and F. Luo, "Design of a high-efficiency, high specific-power three-level T-type power electronics building block for aircraft electric-propulsion drives," *IEEE J. Emerg. Sel. Topics Power Electron.*, vol. 8, no. 1, pp. 407–416, Mar. 2020.
[29] R. V. Chavali, A. Dey, and B. Das, "A hysteresis current controller PWM scheme applied to three-level NPC inverter for distributed generation interface," *IEEE Trans. Power Electron.*, vol. 37, no. 2, pp. 1486–1495, Feb. 2022.
[30] H.-S. Kim, Y.-C. Kwon, S.-J. Chee, and S.-K. Sul, "Analysis and compensation of inverter nonlinearity for three-level T-type inverters," *IEEE Trans. Power Electron.*, vol. 32, no. 6, pp. 4970–4980, Jun. 2017.
[31] Y. Yang, H. Wen, M. Fan, M. Xie, R. Chen, and Y. Wang, "A constant switching frequency model predictive control without weighting factors for T-type single-phase three-level inverters," *IEEE Trans. Ind. Electron.*, vol. 66, no. 7, pp. 5153–5164, Jul. 2019.
[32] Y. Y. Sun, X. M. Xie, Q. Y. Wang, L. H. Zhang, Y. H. Li, and Z. S. Jin, "A bottom-up approach to evaluate the harmonics and power of home appliances in residential areas," *Appl. Energy*, vol. 259, Feb. 2020, Art. no. 114207.
[33] J. Yong, L. Chen, and S. Y. Chen, "Modeling of home appliances for power distribution system harmonic analysis," *IEEE Trans. Power Del.*, vol. 25, no. 4, pp. 3147–3155, Oct. 2010.
[34] Y. H. Chen, Z. Huang, Z. F. Duan, P. W. Fu, G. D. Zhou, and L. F. Luo, "A four-winding inductive filtering transformer to enhance power quality in a high-voltage distribution network supplying nonlinear loads," *Energies*, vol. 12, no. 10, May 2019, Art. no. 2021.
[35] J. Fei and Y. Chu, "Double hidden layer output feedback neural adaptive global sliding mode control of active power filter," *IEEE Trans. Power Electron.*, vol. 35, no. 3, pp. 3069–3084, Mar. 2020.
[36] N. Babu P, J. M. Guerrero, P. Siano, R. Peesapati, and G. Panda, "An improved adaptive control strategy in grid-tied PV system with active power filter for power quality enhancement," *IEEE Syst. J.*, vol. 15, no. 2, pp. 2859–2870, Jun. 2021.
[37] H. G. Wu, B. C. Bao, and Q. Xu, "First order generalized memristor emulator based on diode bridge and series RL filter," *Acta Electronica Sinica*, vol. 43, no. 10, pp. 2129–2132, Oct. 2015.
[38] B. C. Bao, L. Xu, Z. M. Wu, M. Chen, and H. G. Wu, "Coexistence of multiple bifurcation modes in memristive diode-bridge-based canonical Chua's circuit," *Int. J. Electron.*, vol. 105, no. 7, pp. 1159–1169, Dec. 2018.
[39] N. M. Wereley, "Analysis and control of linear periodically time varying systems," Ph.D. dissertation, Dept. Aeronaut. Astronaut., Massachusetts Inst. Technol., Cambridge, MA, USA, 1991.
[40] J. Kwon, X. Wang, F. Blaabjerg, C. L. Bak, V. Sularea, and C. Busca, "Harmonic interaction analysis in a grid-connected converter using harmonic state-space (HSS) modeling," *IEEE Trans. Power Electron.*, vol. 32, no. 9, pp. 6823–6835, Sep. 2017.
[41] J. Lyu, X. Zhang, X. Cai, and M. Molinas, "Harmonic state-space based small-signal impedance modeling of a modular multilevel converter with consideration of internal harmonic dynamics," *IEEE Trans. Power Electron.*, vol. 34, no. 3, pp. 2134–2148, Mar. 2019.
[42] Y. J. Ma, H. Lin, Z. Wang, and Z. Y. Ze, "Stability analysis of modular multilevel converter based on harmonic state-space theory," *IET Power Electron.*, vol. 12, no. 15, pp. 3987–3997, Dec. 2019.
[43] R. I. Leine, D. H. van Campen, and B. L. van de Vrande, "Bifurcations in nonlinear discontinuous systems," *Nonlinear Dyn.*, vol. 23, no. 2, pp. 105–164, Oct. 2000.
[44] A. E. Aroudi, "A new approach for accurate prediction of subharmonic oscillation in switching regulators—Part II: Case studies," *IEEE Trans. Power Electron.*, vol. 32, no. 7, pp. 5835–5849, Jul. 2017.
[45] F. Corinto and A. Ascoli, "Memristive diode bridge with LCR filter," *Electron. Lett.*, vol. 48, no. 14, pp. 824–825, Jul. 2012.
[46] S. P. Adhikari, M. P. Sah, H. Kim, and L. O. Chua, "Three fingerprints of memristor," *IEEE Trans. Circuits Syst. I: Regular Papers*, vol. 60, no. 11, pp. 3008–3021, Nov. 2013.
[47] L. O. Chua, "The fourth element," *Proc. IEEE*, vol. 100, no. 6, pp. 1920–1927, Jun. 2012.

**Hongbo Cao** (Student Member, IEEE) was born in Xianyang, China, in 1993. She received the B.S. degree in electrical engineering and automation from Northwest A&F University, Xianyang, China, in 2016. She is currently working toward the Ph.D. degree in electrical engineering with Xi'an Jiaotong University, Xi'an, China.

Her current research interests include the memristors and its application, modeling and analysis of power electronics.

**Faqiang Wang** (Member, IEEE) was born in Huayuan, Hunan Province, China, in 1980. He received the B.S. degree in automation from Xiangtan University, Xiangtan, China, in 2003, and the M.S. and Ph.D. degrees in electrical engineering from Xi'an Jiaotong University, Xi'an, China, in 2006 and 2009, respectively.

From 2009 to 2011, he was a Lecturer with the School of Electrical Engineering, Xi'an Jiaotong University, where he has been an Associate Professor since 2011. His current research interests include modeling, analysis, and control of power electronics.

**Jinjun Liu** (Fellow, IEEE) received the B.S. and Ph.D. degrees in electrical engineering from Xi'an Jiaotong University (XJTU), Xi'an, China, in 1992 and 1997, respectively.

He then joined the XJTU Electrical Engineering School as a Faculty. From late 1999 to early 2002, he was with the Center for Power Electronics Systems, Virginia Polytechnic Institute and State University, Blacksburg, VA, USA, as a Visiting Scholar. In late 2002, he was promoted to a Full Professor and then the Head of the Power Electronics and Renewable Energy Center, XJTU, which now comprises more than 20 faculty members and more than 200 graduate students and carries one of the leading power electronics programs in China. From 2005 to early 2010, he served as an Associate Dean of Electrical Engineering School, XJTU, and from 2009 to early 2015, the Dean for Undergraduate Education of XJTU. He is currently a XJTU Distinguished Professor of Power Electronics. He coauthored 3 books (including one textbook), authored/coauthored more than 500 technical papers in peer-reviewed journals and conference proceedings, holds more than 70 invention patents (China/US/EU), and delivered for many times plenary keynote speeches and tutorials at IEEE conferences or China national conferences. His research interests include modeling, control, and design methods for power converters and electrified power systems, power quality control and utility applications of power electronics, and microgrids for sustainable energy and distributed generation.

Dr. Liu was a recipient of many times governmental awards at national level or provincial/ministerial level for scientific research/teaching achievements. He was a recipient of the 2006 Delta Scholar Award, the 2014 Chang Jiang Scholar Award, the 2014 Outstanding Sci-Tech Worker of the Nation Award, the 2016 State Council Special Subsidy Award, the IEEE TRANSACTIONS ON POWER ELECTRONICS 2016 and 2021 Prize Paper Awards, and the Nomination Award for the Grand Prize of 2020 Bao Steel Outstanding Teacher Award. He served as the IEEE Power Electronics Society Region 10 Liaison and then China Liaison for 10 years, has been an Associate Editor for IEEE TRANSACTIONS ON POWER ELECTRONICS since 2006, 2015–2019 Executive Vice President and 2020–2021 Vice President of IEEE PELS. He was on the Board of China Electrotechnical Society 2012–2020 and was elected the Vice President in 2013 and the Secretary General in 2018 of the CES Power Electronics Society. He was the Vice President for International Affairs, China Power Supply Society (CPSS) from 2013 to 2021, and since 2016, the inaugural Editor-in-Chief of *CPSS Transactions on Power Electronics and Applications*. He was elected the President of CPSS in November 2021. Since 2013, he has been serving as the Vice Chair of the Chinese National Steering Committee for College Electric Power Engineering Programs.